Constraining the Source Distribution of Meltwater Pulse 1A Using Near- and Far-Field Sea-level Data

by

Jean Paulyn Liu

A thesis submitted in conformity with the requirements
for the degree of Master of Science

Department of Earth Sciences
University of Ottawa

Constraining the Source Distribution of Meltwater Pulse 1A Using Near- and Far-Field Sea-level Data

Jean Paulyn Liu

Master of Science

Department of Earth Sciences
University of Ottawa

2013

Abstract

Meltwater pulse 1A (MWP-1A) is the largest land ice melt event of the last deglaciation. In a period of no more than 340 years, between 14.65 and 14.31 ka (Dechamps et al, 2012), ~10% of the total deglacial sea-level rise occurred (Hanebuth et al, 2000; Peltier and Fairbanks, 2006; Deschamps et al, 2012), resulting in the highest reported rate of global mean sea-level rise in the geological record, which may have exceeded 4 m per century (Deschamps et al, 2012). Yet, the implications of MWP-1A for constraining the rates of the underlying processes and its role in the sequence of climate events during Termination 1 remain unclear due to the lack of information on its melt source distribution. While glacial isostatic adjustment (GIA) modelling experiments (Clark et al, 2002; Bassett et al, 2005; Deschamps et al, 2012) and recent assessments of ice-sheet histories (Carlson and Clark, 2012) suggest that at least 50% of the event may have come from Antarctica, other interpretations of Antarctic ice-extent and sea-level records suggest a substantially smaller (including zero) Antarctic contribution (Ackert et al, 2007; Mackintosh et al, 2011; Whitehouse et al, 2012).

In this study, we show that after reassessments of local MWP-1A amplitudes at Barbados and Sunda Shelf based on the well-constrained timing derived from the Tahiti sea-level record (Deschamps et al, 2012), the sea-level data from Barbados, Sunda Shelf, and Tahiti do not provide as tight of a constraint on the Antarctic contribution as previously thought. We find that between 1 to 10 m sea-level equivalent (sle) could have melted from

the Antarctic, compared to 7 to 15 m sle from previous analyses (Clark et al, 2002; Bassett et al, 2005; Deschamps et al, 2012). To better constrain the source of MWP-1A, we also consider sea-level data from Scotland (Shennan et al, 2000), which have, until now, been excluded from MWP-1A fingerprinting experiments because they are strongly influenced by local ice unloading. To overcome this, we isolate the elastic MWP-1A amplitude (i.e. fingerprint signal) at this location using a suite of models that provide optimal fits to the Scottish data, and thereby remove near-field contamination. Preliminary results show that the inclusion of these data leads to an improved MWP-1A source distribution constraint compared to that obtained using the far- and intermediate-field data alone.

Acknowledgments

I would like to thank my supervisor Glenn Milne for all of his guidance, leadership, and direction. You have taught me so much these past two years. Thank you for taking me on as your student and for letting me work on this incredible project. Thank you for giving me the opportunity to collaborate with some of the leading experts in the field and for encouraging me to present at conferences and always get feedback. You've taught me to aim high and to treat each editing-iteration as a learning experience. I cannot imagine having a better M.Sc. experience.

I would also like to thank Jerry X. Mitrovica, Peter Clark, Bob Kopp, and Ian Shennan for collaboration and/or early feedback. Your insight and expertise are the pillars of this work. I'd also like to particularly thank Peter and Bob for their many hours of email communication, chat sessions, and manuscript edits. I cannot emphasize enough how grateful I am for all of the time and attention you poured into this project.

I would also like to thank Sarah L. Bradley for letting me use her ice model for Chapter 3 of this thesis, as well as many other scientists at the 2012 PALSEA meeting and 2013 PAGES conference for their constructive feedback.

Lastly, I would like to thank the Natural Sciences and Engineering Research Council (NSERC) for funding my research through the Alexander Graham Bell Canada Graduate Scholarship (CGS-M).

Table of Contents

List of Tables

List of Figures

Chapter 1
Introduction

1.1 Meltwater Pulse 1A

Meltwater pulse 1A (MWP-1A) is an episode of large, rapid sea-level rise that occurred between 14.65 and 14.31 ka (Deschamps et al, 2012). It is the largest land ice melt event of the last deglaciation, with ~10% of the total deglacial sea-level rise occurring in a short period of at most 340 years (Deschamps et al, 2012; Peltier and Fairbanks, 2006; Hanebuth et al, 2000). This rapid rate of global mean sea-level rise is the highest reported rate in the geological record, and may even have exceeded 4 m per century (Deschamps et al, 2012).

MWP-1A was first identified from the Barbados sea-level record based on corals, which form reef frameworks within a species-dependent depth below mean sea-level (Fairbanks, 1989; Lighty, 1981) (Section 2.2.1), then subsequently identified in a number of other locations, including Sunda Shelf (Hanebuth, 2001) (Section 2.2.2) and Tahiti (Bard et al, 1996; Deschamps et al, 2012) (Section 2.2.3). This demonstrates that MWP-1A was a global event, though its local relative sea-level (RSL) amplitude differed around the globe.

Identifying the source distribution of MWP-1A is important because it is key to understanding what happened during the last glacial-interglacial transition, as well as what may happen in the future with regards to the mechanisms that govern the Earth's response (solid earth, cryosphere, ocean, and atmosphere) in times of rapid climate change (Section 1.3).

However, the geographical source of MWP-1A remains unknown, with two major conflicting schools of thought: one that argues for a sole Northern Hemispheric source for MWP-1A based on evidence from the near-field (i.e. locations near ice sheets, like the high-latitudes in the Arctic and Antarctic) (Peltier, 2005; Ackert et al, 2007; Mackintosh et al, 2011); and another that argues for a significant Antarctic contribution based on evidence

from the intermediate- and far-field (i.e. locations far from ice sheets, like the Tropics) (Clark et al, 2002; Bassett et al, 2005; Deschamps et al, 2012). Both perspectives are substantiated with evidence, but the nature of the argument requires that only one scenario be true.

1.2 Identifying the Source of MWP-1A

Initially, the North American ice sheets (NAIS), particularly, the Laurentide ice sheet, was assumed to be the sole source of MWP-1A due to its large size (Fairbanks, 1989; Peltier, 1994). However, through a process called sea-level fingerprinting, Clark et al (2002) demonstrated how relative local MWP-1A amplitudes from the far-field preclude a sole North American source for MWP-1A, and suggest a significant Antarctic contribution.

1.2.1 Sea-level Fingerprinting

When ice sheets melt rapidly, sea-level does not rise uniformly around the Earth (Woodward, 1888; Farrell and Clark, 1976). Instead, due to the gravitational forces of massive ice sheets, when an ice sheet melts, sea-level local to the ice sheet may even fall, since an ice sheet with less mass will command a smaller gravitational force (Farrell and Clark, 1976). Therefore, the global sea-level distribution caused by melting solely from the NAIS will look drastically different from that caused by melt solely from the Antarctic ice sheets (AIS) (Figure 1).

Due to this gravitational effect, and other factors like the rebound of the viscoelastic Earth due to load changes and the Earth's rotation (Section 1.5), each melting scenario will generate a unique fingerprint of global sea-level change (Mitrovica et al, 2001). Melting scenarios can then be evaluated against available sea-level records, in a process called the sea-level fingerprinting technique (Mitrovica et al, 2001).

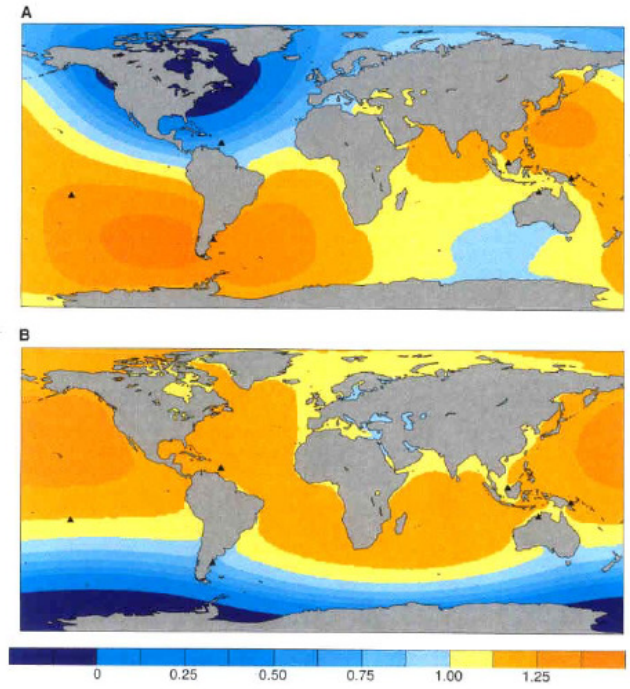

Figure 1: Normalized sea-level change associated with melting from (a) the southern one-third of the Laurentide ice sheet, one of the North American ice sheets, and (b) the West Antarctic ice sheet, one of the Antarctic ice sheets. From Clark et al (2002).

Clark et al (2002) applied this technique and demonstrated that a sole North American source for MWP-1A is not compatible with the RSL rises at Barbados (Bard et al, 1990) and Sunda Shelf (Hanebuth et al, 2000). They found that a sole North American source would have resulted in MWP-1A amplitudes that are ~44% higher at Sunda Shelf than at Barbados (Figure 2), while a significant Antarctic contribution would result in more similar MWP-1A amplitudes (Figure 2). Since the available sea-level evidence at Barbados and Sunda Shelf suggested similar amplitudes of ~25 m at those sites (Clark et al, 2002), they concluded that there must have been a significant Antarctic contribution (Clark et al, 2002).

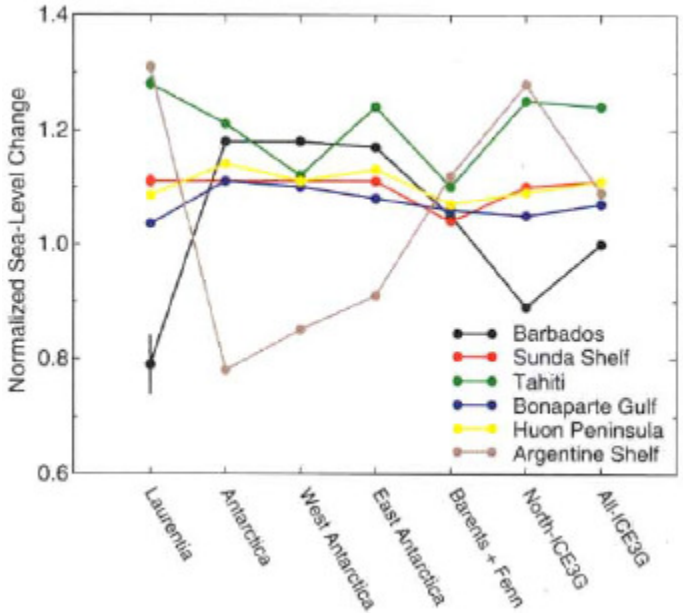

Figure 2: Normalized sea-level change at six far-field sites for seven melting scenarios for MWP-1A. From Clark et al (2002).

In response to Clark et al (2002)'s analysis, however, Peltier (2005) argued that a sole Northern Hemispheric source could not be ruled out since the determination of MWP-1A amplitude in the Barbados and Sunda Shelf sea-level records are highly subject to interpretation and a sole Northern Hemisphere source from his ICE-4G (VM2) deglaciation model could sufficiently satisfy the Barbados and Sunda Shelf sea-level evidence. This deglaciation model, however, faced subsequent criticism for including a Barents-Kara ice sheet contribution after it had already deglaciated (Peltier, 2004) and an over-estimate of Cordilleran ice sheet contribution (Clague and James, 2002).

Bassett et al (2005) built upon this sea-level fingerprinting exercise by considering not only the sea-level rise during MWP-1A, but also the subsequent sea-level rise for 5 ka after it. This made greater use of the available far-field sea-level data, since the post-MWP-1A sea-level change would capture the longer-timescale effect of the rebounding viscoelastic Earth. Consistent with the results of Clark et al (2002), Bassett et al (2005) found that a large Antarctic contribution of ~15 m of sea-level equivalent (m sle) to MWP-

1A would fit the sea-level chronologies at Barbados (Fairbanks, 1989; Bard et al, 1990), Tahiti (Bard et al, 1996), Huon Peninsula (Chappell and Polach, 1991; Cutler et al, 2003), Bonaparte Gulf (Yokoyama et al, 2000), and Sunda Shelf (Hanebuth et al, 2000), without the discrepancies observed when using deglaciation models that include only Northern Hemispheric contributions (Peltier, 2002; Edwards, 1995; Peltier, 1995).

1.2.2 Geological Constraints from Antarctica

Though sea-level fingerprinting studies suggest a large Antarctic contribution to MWP-1A, geological constraints from the Antarctic suggest the opposite – that the Antarctic ice sheets (AIS), instead, contributed very little, if anything at all, to MWP-1A, with most of the melt occurring after MWP-1A (Ackert et al, 2007; Mackintosh et al, 2011),

These interpretations of Antarctic geological constraints, however, are not undisputed. A recent review on possible ice-sheet sources of sea-level rise in the Last Deglaciation argued that a number of factors, including the older reservoir age of dissolved inorganic carbon in the surface mixed layer of the Southern Ocean, may result in large uncertainties in radiocarbon-based chronologies (Carlson and Clark, 2012). After a reassessment of the ice-sheet histories in both the Northern Hemisphere and the Antarctic, the authors proposed alternate interpretations of the Antarctic geologic constraints, and concluded that although the rates of deglaciation are not well-constrained, the widespread signature of Antarctic ice retreat between 14-15 ka is consistent with a significant Antarctic contribution to MWP-1A (Carlson and Clark, 2012).

This conclusion is also supported by recent evidence from two deep-sea sediment cores positioned in the centre of the iceberg alley, in the central Scotia Sea (Weber et al, 2013). According to the study, the two sediment cores provide representative means to reconstruct entire AIS disintegration during the last deglaciation since 90% of all Antarctic icebergs would have passed through this region. The timing of highest peak in ice-rafted debris (IRD) flux in this record, which they call Antarctic Ice Sheet Disintegration phase 3 (AID 3), occurred between 14.76 to 14.4 ka (Weber et al, 2013). This is consistent with the

recent dating of between 14.65 and 14.31 ka from the high-resolution Tahitian coral chronology (Deschamps et al, 2012). Analysis of the evidence from the central Scotia Sea suggests that there was up to 7 times more iceberg flux during AID 3 than the Holocene steady-state average; however, the authors make very clear that they are far from being able to constrain the actual volume of Antarctic melt.

1.3 Implications

The existing body of evidence leaves us with a baffling contradiction regarding the source of MWP-1A. Sea-level fingerprinting experiments based on far-field sea-level data and sophisticated geophysical models, thus far, seem to suggest a significant Antarctic contribution (Clark et al, 2002; Bassett et al, 2005), but the majority of studies based on near-field geological evidence seem to suggest the opposite – that the AIS contributed very little, with most of the melt occurring after MWP-1A (Ackert et al, 2007; Mackintosh et al, 2009). Though a recent reassessment of the Antarctic geological constraints (Carlson and Clark, 2012) and new evidence of increased IRD flux in the central Scotia Sea (Weber et al, 2013) suggest that there may have been a larger AIS contribution to MWP-1A than suggested by past near-field geological studies, the current state of the debate is that the source distribution of MWP-1A is still disputed and unresolved.

Resolving the apparent contradictions between the far-field sea-level data and near-field geological constraints and identifying the source of MWP-1A is key to understanding both what happened in the past, during the last glacial-interglacial transition (Section 1.3.1), as well as what may happen in the future, and the mechanisms that govern the Earth's response (solid earth, cryosphere, ocean, and atmosphere) in times of rapid climate change (Section 1.3.2).

1.3.1 Understanding the Last Glacial-Interglacial Transition

MWP-1A occurred during the last glacial-interglacial transition, which is marked by a rapid warming event in the Northern Hemisphere, called the Bølling-Allerød interstadial (Deschamps et al, 2012), that is attributed to the reinvigoration of North Atlantic Deepwater (NADW) formation in the Nordic Seas from a reduced state compared to present-day levels (Charles and Fairbanks, 1992; Lehman and Keigwin, 1992). This reinvigoration in NADW formation reflects the strengthening of a large-scaled density driven pattern of ocean circulation in the North Atlantic, called the thermohaline circulation (THC) (Fig 3), which is responsible for warming the North Atlantic, specifically northern Europe (Broecker, 1987).

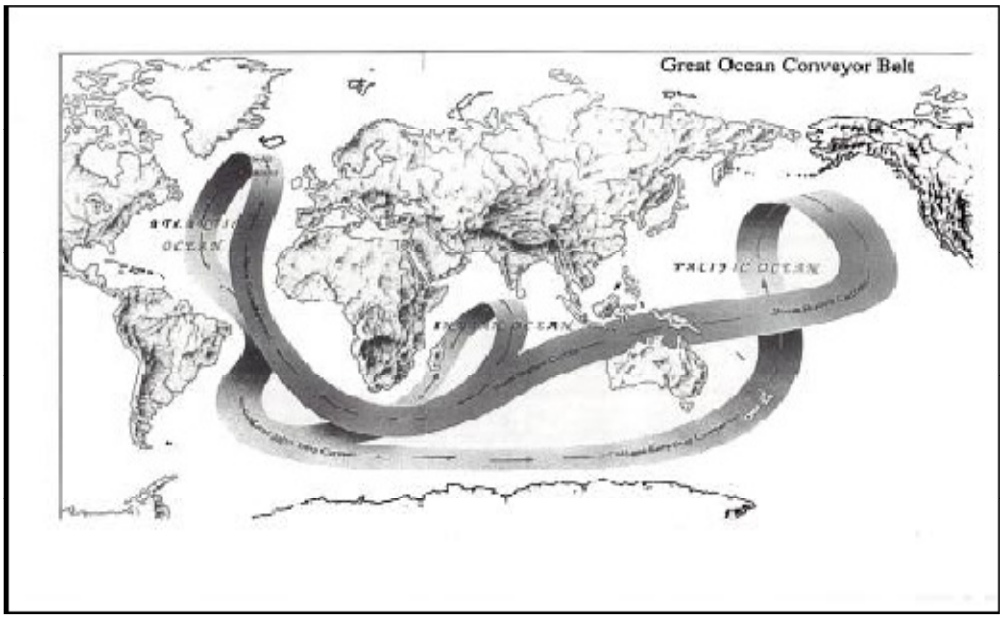

Figure 3: Thermohaline Circulation and the Great Ocean Conveyor Belt. From Broecker (1987).

The THC operates by transporting warm, high salinity surface waters from the Tropics northwards. As it cools, the water becomes more dense and sinks, forming deepwater in the North Atlantic. This cold deepwater from the North Atlantic then flows southwards, completing the “great oceanic conveyor belt” (Broecker, 1987). It is the warming of the North Atlantic air by transport of warm surface water by the THC, and the

carrying of this air by the Northern Hemisphere westerlies that warms northern Europe in comparison to other regions at the same latitude (Broecker, 1987).

The timing of start MWP-1A has been recently well-constrained to the timing of the Bølling warming, and thus coincident with the reinvigoration of the THC. However, the sequence of events is still poorly understood. One study by Weaver et al (2003) suggests that the partial collapse of an ice sheet may have been the cause of the THC reinvigoration, which then caused the Bølling warming. By applying freshwater forcings to a global climate model, Weaver et al (2003) shows that the THC can be reinvigorated by a melting event in the Antarctic, but not by reducing Northern Hemisphere freshwater input to zero and waiting a few thousand years. This supports the argument for a significant Antarctic contribution to MWP-1A. However, the above conclusion is controversial, and others have suggested that the THC can resume due to wind-driven circulation, after freshwater forcing (i.e. melting of Northern Hemisphere ice sheets) stops (Peltier, 2005).

As such, independently identifying the source of MWP-1A will help identify the cause of the THC reinvigoration during the Bølling warm period, as well as the climate linkages that exist between the cryosphere, oceans, and atmosphere. However, understanding these mechanisms is also important in testing and refining models used to predict future climate change.

1.3.2 Constraining Models of Future Climate

In order to constrain models for future climate change, we need to understand how the Earth (solid earth, atmosphere, oceans, and cryosphere) responds in periods of rapid sea-level rise. Future sea-level projections differ by an order of magnitude, ranging between 2 to 13 mm/year (Willis et al, 2010). Since MWP-1A is the largest, fastest sea-level rise recorded in geological history, it is a useful event to consider, when examining for mechanisms, feedbacks, and possible tipping points associated with rapid sea-level rise, and addressing the question of whether a similar rate of sea-level rise can occur in the future. Identifying the source distribution for MWP-1A can also help identify ice sheet instabilities and revealing

the glaciological processes and mechanisms that can result in such a catastrophic sea-level rise. This has implications for understanding and predicting contemporary and future mass loss from the Arctic and Antarctic.

1.4 Outline of Thesis

The principal objective of this thesis is to build upon the sea-level fingerprinting analysis of Clark et al. (2002) by considering new near- and far-field evidence relating to the MWP-1A source problem as well as applying more sophisticated modeling techniques and a more careful assessment of data uncertainty. In addition, we expand upon their method by also considering sea-level data from a near-field region (Scotland) in an attempt to increase data control and thus better constrain the problem.

We consider a number of recent deglaciation models, including: a glaciologically-self-consistent model for the AIS that is constrained by near-field geological and glaciological proxies for ice-sheet thickness, as well as marine sediment cores and geophysical evidence of past grounded ice extent (Whitehouse et al, 2012). We also consider two very different deglaciation models for the NAIS: a surface mass-balance model forced by an atmosphere-ocean general circulation model (AOGCM) (Carlson et al, 2012) and a glaciologically-self-consistent model calibrated with near-field RSL, marine limit, and geodetic data (Tarasov et al, 2012).

In Chapter 2, we test this suite of 40,000 melting scenarios against sea-level evidence at three intermediate- and far-field sites: Barbados (Fairbanks and Peltier, 2006), Sunda Shelf (Hanebuth et al, 2000), and Tahiti (Deschamps et al, 2012). This is an improvement upon past studies since we include our own reassessments and corrections to the sea-level data at Barbados (Fairbanks and Peltier, 2006) and Sunda Shelf (Hanebuth et al, 2000), which will be described in Section 2.2, as well as evidence from the new data-rich Tahitian coral record (Deschamps et al, 2012).

In Chapter 3, we will explore a novel approach whereby we incorporate data from a near-field sea-level site: Arisaig, Scotland (Shennan et al, 2000). Until now, sea-level

constraints from near-field sites have been excluded from MWP-1A fingerprinting experiments because they are strongly influenced by local ice unloading. To overcome this, we isolate the elastic MWP-1A amplitude (i.e. fingerprint signal) at this location using a suite of models that provide optimum fits to the Scottish data, thereby removing near-field contamination. We will describe this new technique in detail, then show that the inclusion of these near-field data leads to an improved MWP-1A source distribution constraint compared to that obtained using the intermediate- and far-field data alone.

1.5 Theory

In this thesis we use the sea-level algorithm of Kendall et al (2005) and the improved treatment of the earth rotation feedback by Mitrovica et al (2005). We define changes in the sea-level as the difference between changes in height of the ocean surface, or geoid, and changes in the surface of the solid Earth:

$$S(\theta,\psi,t) = C(\theta,\psi)[G(\theta,\psi,t) - R(\theta,\psi,t)] \quad (1)$$

where C is the ocean function, defined as unity over the oceans, $G(\theta,\psi,t)$ is the change in the height of the geoid defined globally, and $R(\theta,\psi,t)$ is the change in the height of the Earth's solid surface, defined globally.

The change in geoid height $G(\theta,\psi,t)$ can be further deconstructed into the sum to two terms: one that represents a spatially-uniform height shift in the geoid, and another that varies spatially around the globe:

$$G(\theta,\psi,t) = \frac{1}{g}\Phi(\theta,\psi,t) + G(t) \quad (2)$$

where g is the mean surface gravitational acceleration, $\Phi(\theta,\psi,t)$ is the gravitational potential, and $G(t)$ is the spatially-uniform height shift in the geoid, defined as:

$$G(t) = -\frac{M_I(t)}{\rho_w A_o} - \frac{1}{A_o} < G(\theta,\psi,t) - R(\theta,\psi,t) > \quad (3)$$

where $M_I(t)$ is the total mass of ice sheets melted, ρ_w is the density of water, A_o is the area of the oceans, and the angle brackets denote a spatial integration over the oceans.

Combining these equations, we get the following formula for sea-level change:

$$S(\theta,\psi,t) = C(\theta,\psi)\left[\frac{1}{g}\Phi(\theta,\psi,t) - R(\theta,\psi,t) - \frac{M_I(t)}{\rho_w A_o} - \frac{1}{A_o} < G(\theta,\psi,t) - R(\theta,\psi,t) >\right] \quad (4)$$

In the above sea-level equation (Eq 4), the first term represents the gravitational component of sea-level rise, which has two parts: a direct gravitational effect and an indirect gravitational effect. The direct gravitational effect is associated with redistributions in mass between the cryosphere and oceans. For example, as mentioned in Section 1.2.1, when an ice sheet melts, local sea-level may even fall because ice sheets with less mass command a smaller gravitational force (Farrell and Clark, 1976) (Fig 4).

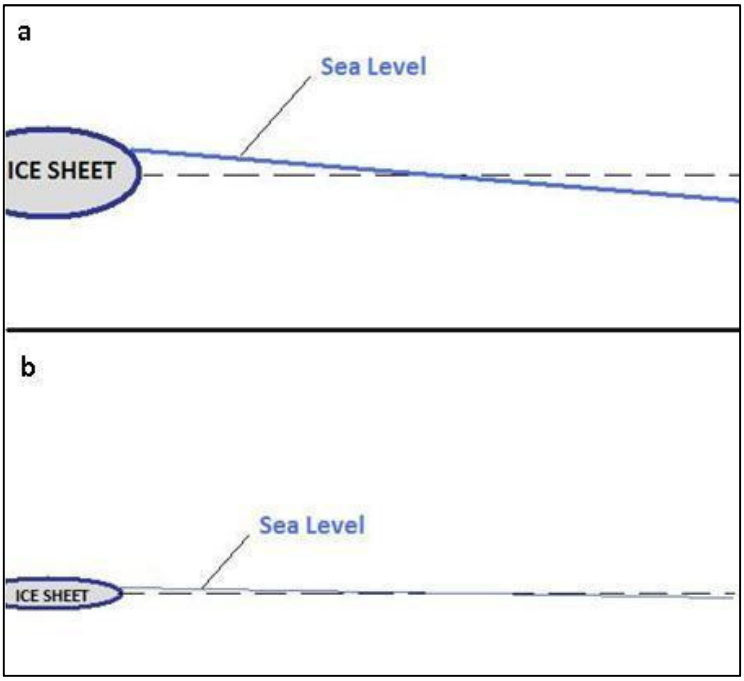

Figure 4: Direct gravitational effect caused by the melting of an ice sheet: (a) before and (b) after.

The indirect gravitational effect, on the other hand, is caused by the mass loading redistribution associated with the solid earth deformation that occurs in response to the ice-

ocean mass redistribution (Farrell and Clark, 1976). Both the direct and indirect gravitational effects also include changes in the Earth's gravitational potential that are associated with changes in the rotational potential caused by the spatial redistributions of mass between the ice and oceans, or due to mantle flow, respectively.

The second term in Equation 4 represents the solid earth response to ice-ocean mass loading redistribution, or in other words, resultant changes in the height of the Earth's solid surface. This solid earth response can be described in terms of two key phenomena: (1) the viscoelastic rebound of previously-glaciated or deglaciating regions, called post-glacial rebound, and (2) the subsidence of the peripheral bulge associated with past ice sheets (Fig. 5 and 6).

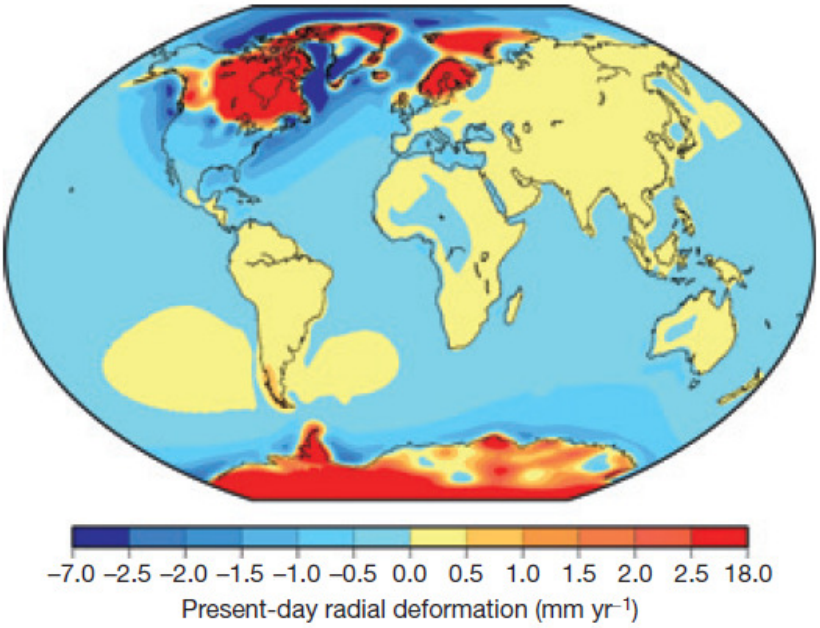

Figure 5: Key phenomena governing the solid earth response to deglaciation: (1) sea-level fall due to the viscoelastic rebound of previously-glaciated or deglaciating regions, and (2) sea-level rise due to the subsidence of the peripheral bulge. From Milne and Shennan (2013).

Because ice sheets are massive, they deform the solid earth beneath them and form peripheral bulges (Fig 6a). When ice sheets melt, the mass load is reduced, so the solid earth beneath the former ice sheet rebounds and the peripheral bulges subside, over time (Fig 6b).

Because sea-level is defined as the difference between the ocean surface and ocean floor, this results in a local sea-level fall in the region directly beneath the former ice sheets (Fig 5) and a sea-level rise in the region of the peripheral bulge (Fig 5) compared with the case where there is no solid earth deformation.

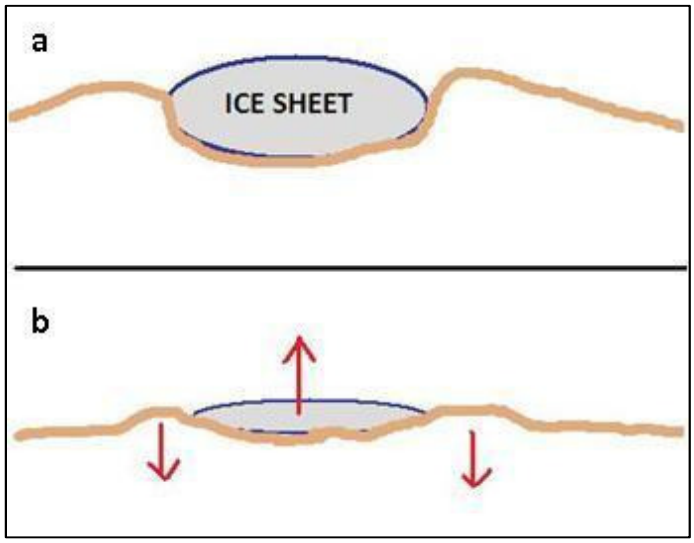

Figure 6: Post-glacial rebound and the subsidence of the peripheral bulge: (a) before deglaciation, and (b) after deglaciation.

Since the earth is viscoelastic, the solid earth response has two components: an effectively-immediate elastic response and a slower viscous response. In Chapter 2, we show that the elastic component dominates the response to MWP-1A in the intermediate- and far-field sites: Barbados, Sunda Shelf, and Tahiti. So, in Chapter 2, we can neglect the viscous component of the response across the MWP-1A time window of 340 years (Deschamps et al, 2012). However, in Chapter 3, we demonstrate that the viscous component is important in Arisaig, Scotland – a near-field site – and describe a novel technique for removing this component to isolate the fingerprint signal (which is caused by only elastic deformation and direct gravitational effects).

The third term in Equation 4 represents the eustatic sea-level rise, which is the amount of sea-level rise we would get simply by melting the ice and transferring the water to the oceans uniformly. It is simply an expression of the conservation of mass.

Finally, the fourth term in Equation 4 is the non-eustatic component of the spatially-uniform sea-level change, associated with changes in ocean volume caused by a number of GIA-induced effects, including the collapse of marine-based components of continental ice sheets, peripheral bulge subsidence, and ocean-loading effects (Mitrovica and Milne, 2002). For, example, one non-eustatic effect, is caused by the siphoning of far-field (i.e. Tropical) oceans in order to fill volumes vacated by the subsiding peripheral bulge (Fig 6). This effect results in mid-Holocene sea-level highstands in which local sea-levels in far-field oceans exhibit a gradual sea-level rise until ~5 ka BP, followed by a gradual sea-level fall caused by the sea-level siphoning effect.

For simplicity, in the following chapters, we categorize the above described components of sea-level change into two classifications: (1) the elastic component, which encompasses all of the instantaneous (short timescale) responses, i.e. the direct gravitational effect, the elastic solid earth response, and the eustatic component of sea-level rise; and (2) the viscous component, which encompasses the long time-scale responses, i.e. the viscous component of ocean floor height change and the indirect gravitational effect associated with the viscous deformation over the globe. In the following chapters, unless otherwise specified, the elastic component and viscous component will refer to the sum of these above-listed corresponding effects, not just the elastic and viscous components of the solid earth response.

Chapter 2
Constraining the Source of MWP-1A Using More Realistic Melting Scenarios and Reassessed Far-Field Data

2.1 Melting Scenarios and Spatial Melting Functions

In the following sea-level fingerprinting experiment, we test a suite of 40,000 melting scenarios that are linear combinations of nine spatial melting functions based on the best fit results of near-field models of the Antarctic ice sheets (Whitehouse et al, 2012), North American ice sheets (NAIS) (Carlson et al, 2012; Tarasov et al, 2012), Fennoscandian ice sheet (FIS) (Lambeck et al, 1998), and Greenland ice sheet (GIS) (Simpson et al, 2009). Since the focus of this analysis is the AIS and NAIS, a handful of spatial functions are considered for these ice complexes. These are based on common elements from different deglaciation models and so are relatively robust.

2.1.1 Antarctic Ice Sheets

The AIS contribution to MWP-1A is defined using 4 spatial weighting functions – one for each of Wilkes Land, Weddell Sea, Ross Sea, and the Antarctic Peninsula (Fig 7). These are based on the spatial distribution of ice volume change between 15 and 10 ka BP in the glaciologically-consistent model of Whitehouse et al (2012). Although this would include ice volume changes from after MWP-1A (~14.3 ka BP) to 10 ka BP, personal communication with the authors of the paper confirms that they have no major objections to approximating the Antarctic contribution in this way, and the defined spatial functions are consistent with the regions of possible melt contribution between 15 and 14 ka BP in a very different deglaciation model by Mackintosh et al (2011).

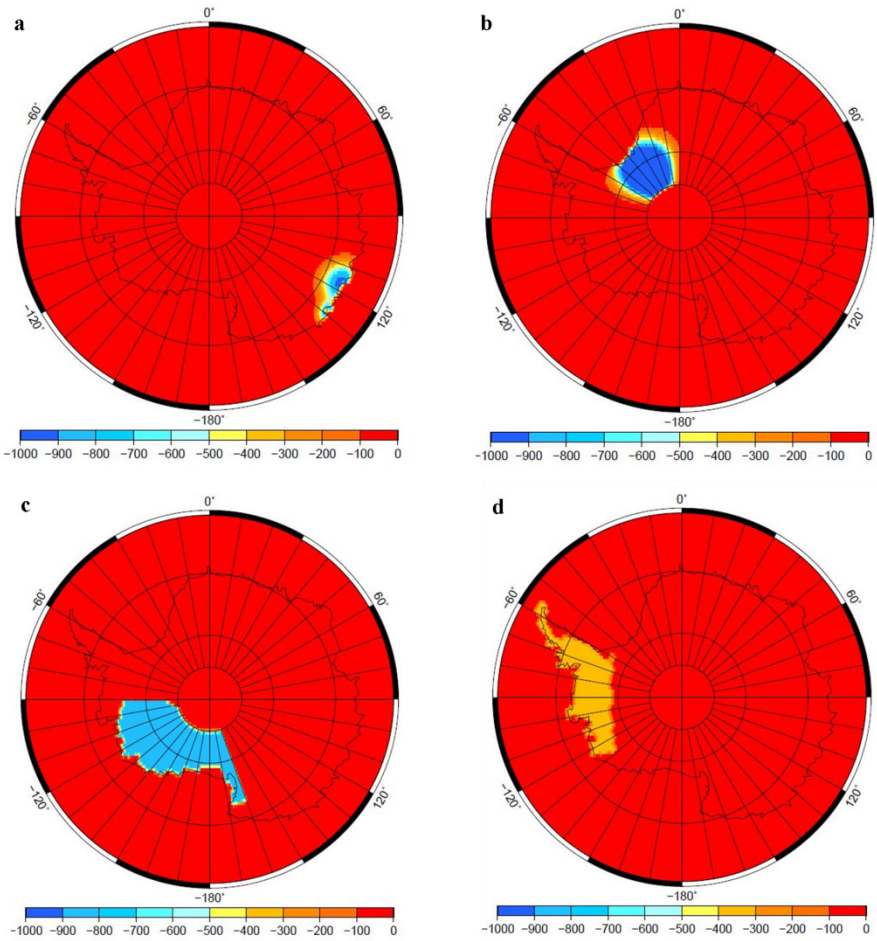

Figure 7: Antarctic spatial melting functions. Volume of ice melted from: (a) Wilkes Land, (b) Weddell Sea, (c) Ross Sea, and (d) Antarctic Peninsula. More negative values (blue) indicate more melt. Each spatial melting function is scaled for total regional contribution volumes, as described in Section 2.1.4, so figure scale is unimportant.

In order to avoid having our results depend too heavily on the Whitehouse et al (2012) model for Antarctic deglaciation, we define our spatial melting functions more generally, in a way that is also consistent with the deglaciation model of Mackintosh et al (2011). We model the spatial melting function over Wilkes Land (Fig 7a) as the sum of two Gaussian distributions over the ice volume available at 14.5 ka BP in ICE5G (Peltier, 2004), and define the spatial melting function over the Weddell Sea (Fig 7b) as a single Gaussian over the ice volume available at the same time in the same ice model. The Ross Sea and Antarctic Peninsula spatial melting functions (Figure 7c and d), however, we model as

uniform distributions over the available ice volumes at 14.5 ka BP in ICE5G, based on the spatial melt distributions observed in Whitehouse et al (2012)'s model.

Though we choose to use non-uniform spatial melting functions to represent the ice volume loss in Wilkes Land and the Weddell Sea (Fig 8), the results, as we will show in Section 2.3.3 are insensitive to the type of weighting functions used. Repeating the fingerprinting experiment using only uniform spatial melting functions gives identical constraints MWP-1A source distribution.

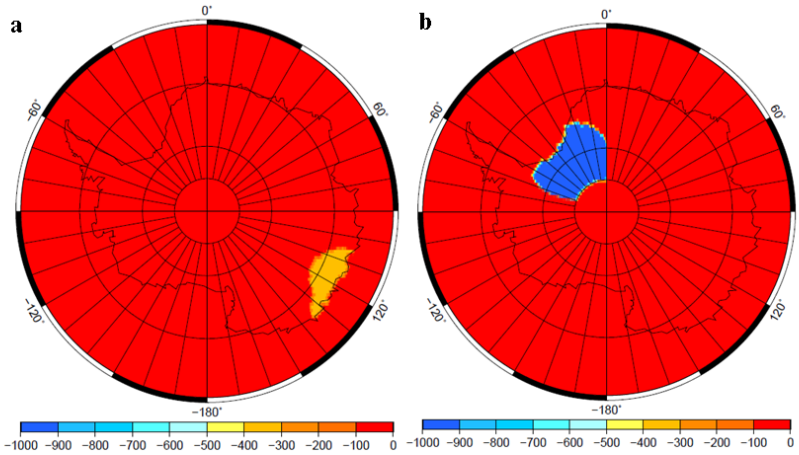

Figure 8: Alternative spatial melting functions for (a) Wilkes Land, and (b) Weddell Sea. More negative values (blue) indicate more melt. Each spatial melting function is scaled for total regional contribution volumes, as described in Section 2.1.4, so figure scale is unimportant.

2.1.2 North American Ice Sheets

For the NAIS, we define 3 spatial melting functions based on two very different deglaciation models (Carlson et al, 2012; Tarasov et al, 2012). The first of these, the Carlson et al (2012) model, simulates the surface-mass balance response of the NAIS to Bølling warming, as forced by an AOGCM. It predicts significant mass loss in the northwestern margin of the Laurentide ice sheet (LIS), as well as a broader alternation of mass loss and mass gain across the rest of the ice sheet. We define two spatial melting functions (Fig 9a and b) that approximate each of these.

The second model we consider is the Tarasov et al (2012) model, which is glaciologically-self-consistent and calibrated against RSL, marine limit, and geodetic data. It predicts a large signal of mass loss due to the cleaving of the two main ice sheets of the NAIS complex: the LIS and Cordilleran ice sheet (CIS), consistent with the saddle collapse mechanism described by Gregoire et al (2012). We approximate this signal using one spatial melting function over the NAIS-LIS boundary (Fig 9c).

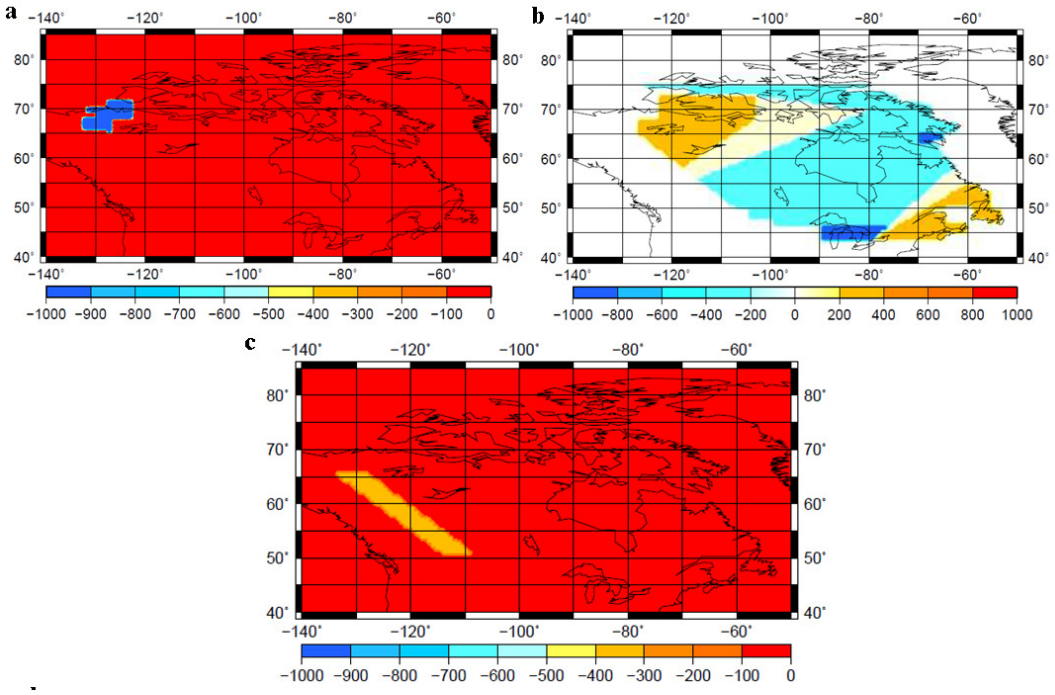

Figure 9: NAIS spatial melting functions. Volume of ice melted from: (a) the northwest of the NAIS, (b) the broader mass loss and gains across the NAIS, and (c) the saddle collapse separation of the CIS and LIS. More negative values (blue) indicate more melt. Each spatial melting function is scaled for total regional contribution volumes, as described in Section 2.1.4, so figure scale is unimportant

Just as is the case with the AIS, the results of the fingerprinting experiment are insensitive to the type of melting functions we use (Section 2.3.3). When we repeat the experiment using only uniform spatial melting functions across the LIS (Fig 9c; Fig 10), we get identical constraints on the MWP-1A source distribution (Section 2.3.3).

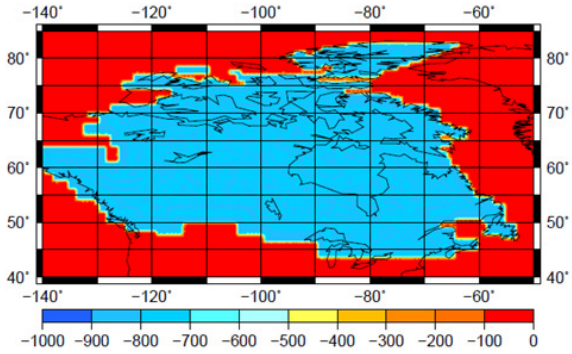

Figure 10: Alternative spatial melting function for the NAIS. More negative values (blue) indicate more melt. Each spatial melting function is scaled for total regional contribution volumes, as described in Section 2.1.4, so figure scale is unimportant.

2.1.3 Greenland and Fennoscandian Ice Sheets

The final two spatial melting functions describe the melt across the GIS and FIS, respectively (Fig 11). These are based on the best-fit model of the GIS by Simpson et al (2009) and the best-fit model of the FIS by Lambeck et al (1998). The contributions of these ice sheets are quite small compared to the global MWP-1A source, with 1.1 m sle from the FIS and 0.2 m sle from the GIS, according to these models. Because these contributions are small and because these models are not under much dispute, we take the spatial melting functions directly from the referenced reconstructions.

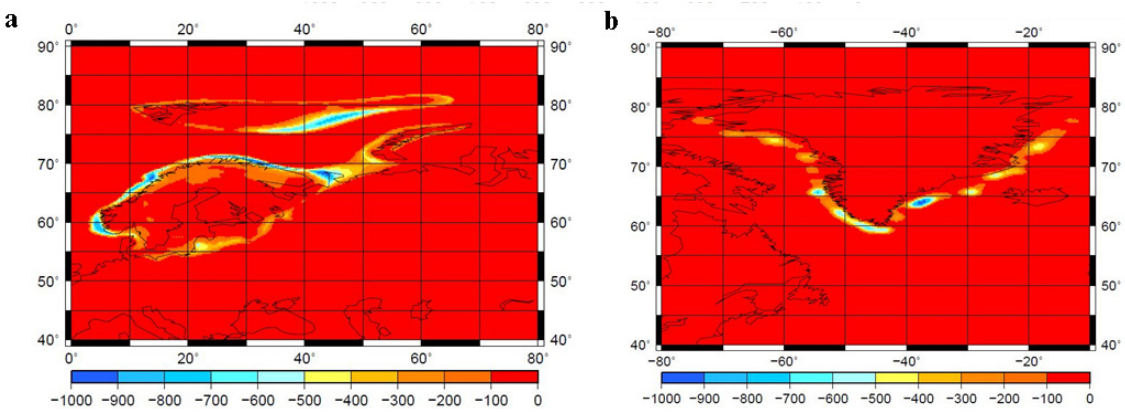

Figure 11: Spatial melting functions for the (a) FIS and (b) GIS. More negative values (blue) indicate more melt. Each spatial melting function is scaled for total regional contribution volumes, as described in Section 2.1.4, so figure scale is unimportant.

2.1.4 Scaling Spatial Melting Functions

To generate a suite of 40 000 melting scenarios for our fingerprinting experiment, we scale our spatial melting functions so that the contributions from each is between zero and twice the maximum melt contribution cited in the source literature (Table 1). We conservatively consider melt contributions of up to twice the upper limit in the literature in order to help account for differences in the interpretation of near-field data. This is done for all spatial melting functions except the saddle collapse signal (Fig 9c), where instead we limit mass loss to 15 m sle. The nine spatial melting functions are then scaled pseudo-randomly. First, the total AIS and NAIS contributions are sampled with uniform distribution, then the relative weight of each sub-ice sheet spatial function is sampled from a uniform distribution. This is done 40,000 times to generate 40,000 melting scenarios.

Table 1: Standard (column 4) and narrow (column 5) scaling ranges for sectoral ice melt.

Ice Sheet	**Spatial Weighting Function**	**Corresponding Figure**	**Max Value Sampled in Standard Range (m sle)**	**Max Value Sampled in Narrow Range (m sle)**
AIS	Wilkes Land	Figure 7a	2.0	1.0
	Weddell	Figure 7b	2.4	1.2
	Ross	Figure 7c	3.0	1.5
	Peninsula	Figure 7d	2.8	1.4
NAIS (Carlson et al, 2012)	Localized signal in Northwest	Figure 9a	3.8	1.9
	Broader signal of regional mass losses and gains	Figure 9b	13.6	6.8
NAIS (Tarasov et al, 2012)	"Saddle collapse" separating LIS and CIS	Figure 9c	15.0	13.2
FIS	Full signal	Figure 11a	2.2	1.1
GIS	Full signal	Figure 11b	0.4	0.2

Though we choose to scale our melting functions between 0 and twice the upper bound in literature, in Section 2.3.3, we show that we get very similar results when using a

narrower range of AIS and NAIS melt contributions where we scale only between zero and the maximum melt contribution suggested in the source literature (Table 1, column 5).

2.2 Intermediate- and Far-Field Data

We test the above-described melt scenarios against the local MWP-1A amplitudes derived from RSL data at three intermediate- and far-field sites Barbados (Peltier and Fairbanks, 2006), Sunda Shelf (Hanebuth et al, 2000), and Tahiti (Deschamps et al, 2012). In the sections below, we describe the sea-level data we use, as well as the corrections and reassessments we make to the MWP-1A amplitudes.

2.2.1 Barbados

MWP-1A was first identified from the Barbados sea-level record, which is defined by corals (Peltier and Fairbanks, 2006). Since corals grow within a species-specific range below mean sea level, the depth and age of several coral samples from a location can be used to create a local sea-level chronology (Lighty, 1981). By assuming that the corals were able to grow during periods of rapid sea-level rise, Peltier and Fairbanks (2006) estimated that MWP-1A occurred between 14.2 ka and 13.5 ka and had an RSL amplitude of 14 to 24 m.

However, corals do not always keep up with rapid sea-level rises (Neumann et al, 1985). Instead, sometimes they drown below their livable range. Weaver et al (2003) point out that this may have been the case for the coral samples used by Peltier and Fairbanks (2006) to constrain the timing and amplitude of MWP-1A. They point out that the sample of the shallow-water coral species (*Acropora palmata)* that is commonly used to define the start of the event at 14.2 ka is directly overlain by deeper water coral species. This suggests that the shallow-water corals (Fig 12, purple) were already in the process of drowning following an increase in the rate of sea-level rise (Neumann et al, 1985; Weaver et al, 2003).

A high-resolution coral record from Tahiti confirms this earlier start of MWP-1A, as well as an older end, with the event occurring between 14.65 ka and 14.31 ka (Deschamps et al, 2012). With this new chronology, Deschamps et al (2012) reassessed the amplitude of MWP-1A in the Barbados sea-level record by extrapolating backwards in time from the first dated *A. palmata* sample after MWP-1A to the end of the MWP-1A period as defined by the Tahitian corals (Fig 12, dotted green line).

We assign an uncertainty to this reassessed Barbados MWP-1A amplitude (Deschamps et al, 2012) using the depth (Peltier and Fairbanks, 2006) and age (Peltier and Fairbanks, 2006; Reimer et al, 2009) uncertainties of the coral samples during and after the MWP-1A time window defined from Tahiti (Fig 12). We set a maximum RSL for the end of MWP-1A using the lowest slope (blue dotted line) that is consistent with *A. palmate* samples RGF-12-21-6 and RGF-12-14-4 (orange points), and a minimum RSL using the steepest slope (red dotted line).

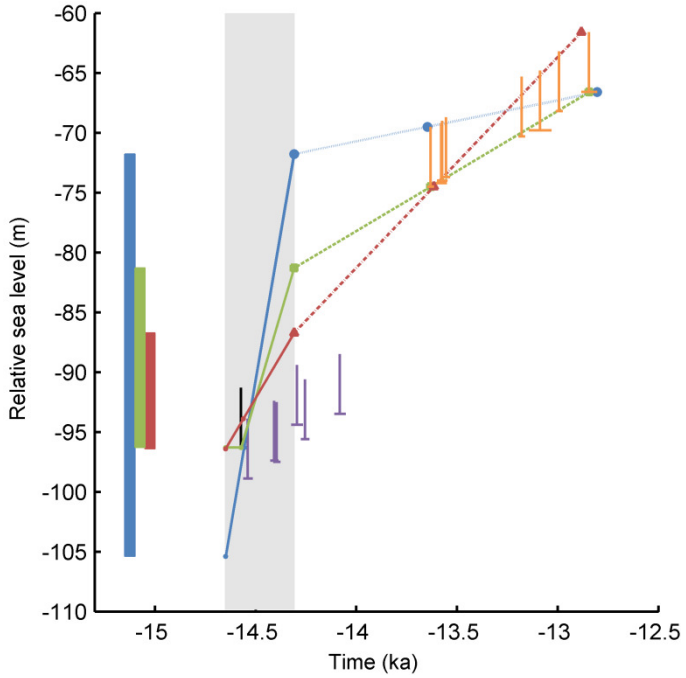

Figure 12: MWP-1A amplitude reassessed at Barbados using age and depth uncertainties in coral samples. Horizontal bars denote age uncertainties and hard lower bounds. Vertical bars denote depth uncertainties. Purple points are from site 9, orange from Site 12, and black from site 15 of Fairbanks and Peltier (2006). Grey box denotes MWP-1A timing based on the Tahitian record of Deschamps et al (2012). Blue bar denotes maximum local MWP-1A amplitude, red bar denotes minimum local MWP-1A amplitude, and green bar denotes the local MWP-1A amplitude suggested by Deschamps et al (2012).

Since samples RGF-15-5-3 (Fig 12, black point) and RGF-9-13-3 (earliest purple point) are the same age within uncertainty, we define the overlap in depths and ages as our earliest data constraint and extrapolate back to 14.65 ka, the beginning of the MWP-1A period (Deschamps et al, 2012), to get the RSL for the start of the MWP-1A period (solid blue, green, and red lines).

We thus reconstrain the RSL amplitude of MWP-1A at Barbados to between 10 and 34 m (Fig 12, red and blue bars). We consider the full range between the minimum and maximum MWP-1A amplitude in order to remain conservative in our local Barbados constraint. However, because the duration of MWP-1A from the Tahiti record could be shorter (Deschamps et al, 2012), this approach results in upper bounds for both the maximum and minimum RSL amplitudes.

2.2.2 Sunda Shelf

The sea-level record at Sunda Shelf (Hanebuth et al, 2000) is defined by mangroves which, like corals, grow in a specific elevation range relative to mean sea-level. Assuming that all the core sites represent a single sea-level location suggests that MWP-1A had a RSL amplitude of 12 to 20 m and occurred at the same time as it did in Tahiti (Hanebuth et al, 2000) (Fig 13b). However, there is a considerable sea-level gradient across the region due to hydroisostasy (Lambeck et al, 2002) (Fig 13a), which influences the estimated MWP-1A amplitude since the core locations are not tightly grouped.

To account for this gradient and thus arrive at a more accurate estimate of MWP-1A amplitude, we use a geophysical sea-level model to translate all of the Sunda Shelf sea-level observations to their equivalent values at a single location (Fig 13a, black star). We calculate the sea-level at each of our Sunda Shelf core sites using the sea-level algorithm of Kendall et al (2005) with an improved treatment of the earth rotation feedback (Mitrovica et al, 2005) (Section 1.5). In order to be conservative in our estimation of the model uncertainty,we consider a broad range of parameter values, namely a suite of 324 model runs using two ice

models – ICE5G (Peltier, 2004) and that of Bassett et al (2005) – and 162 combinations of earth model parameters – lithosphere thickness of 71, 96, and 120 km; upper mantle viscosity of 0.1, 0.2, 0.3, 0.5, 0.8, and 1 x 10^{21} Pas; and lower mantle viscosity of 1, 2, 3, 5, 8, 10, 20, 30, and 50 x 10^{21} Pas.

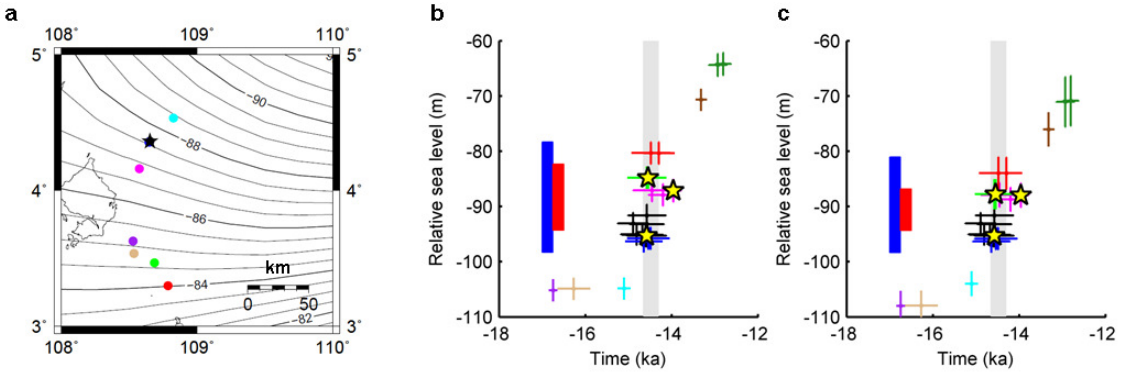

Figure 13: Spatial sea-level gradient correction for the Sunda Shelf study region. (a) Sea-level isochrons across Sunda Shelf in mean of model ensemble. Black star denotes site 18300 – to which all other sites are reduced; cyan dot marks site 18299, blue 18301, magenta 18302, purple 18307, red 18308, green 18309, and tan 18310. (b) and (c) show relative sea-level constraints at Sunda Shelf before and after the spatial correction is made, with colours corresponding to different core sites as defined in (a) and yellow stars marking in-situ samples. Horizontal bars mark age uncertainty. Vertical bars mark depth uncertainty, which includes GIA model uncertainty in (c). Grey box denotes MWP-1A timing (Deschamps et al, 2012).

The model results indicate a 2 to 4 m sea-level difference in the sites that define the RSL at the beginning (Fig 13a, blue dot) and end (Fig 13a, red dot) of MWP-1A. Correcting for the sea-level gradient across all the data points, we define the spatial correction using the mean difference between the sea-level at each core location and that at core site 18300. We use the associated 2σ error, to define a spatial correction that includes model uncertainty for each raw data point (Hanebuth et al, 2000), calibrated with IntCal09 (Reimer et al, 2009), around MWP-1A (Fig 13c). In doing so, we reduce our Sunda Shelf data to a single location (core site 18300, 4.3630° N, 108.6536° E) and find a revised MWP-1A amplitude of 7.5 to 17.3 m at Sunda Shelf (4.3630° N, 108.6536° E), compared with 12 to 20 m for the uncorrected data.

2.2.3 Tahiti

The recent high-resolution coral record from Tahiti yields a local MWP-1A RSL amplitude of 12 to 22 m, which represent the lowermost and uppermost bound on the local sea-level jump (Deschamps et al, 2012). Deschamps et al (2012) suggest that this range can even be reasonably narrowed down to a *more probable* range of 14 to 18 m, but to be consistent with the conservative nature of this study, we adopt the 12 to 22 m range, though in Section 2.3.5, we show that our constraints on MWP-1A source distribution are insensitive to our choice between the narrower versus broader Tahiti MWP-1A amplitude range. We adopt this amplitude explicitly to provide a local MWP-1A constraint in our sea-level fingerprinting experiment. In addition to this, as illustrated in Sections 2.2.1 and 2.2.2, we also use this data set to define the timing of MWP-1A, which also represents an upper bound on MWP-1A duration, however, in this study, we choose to define MWP-1A as the melt that occurs between 14.31 and 13.65 ka, thus assuming that the timing is the same across our study sites since ocean dynamic effects across these sites are small (~15 to 30 cm) (He, 2010).

2.3 Sea-level Fingerprinting

We now test our 40,000 melting scenarios against the observed local MWP-1A amplitudes at our three intermediate- and far-field sites. We use a static sea-level model based on, again, the sea-level algorithm of Kendall et al (2005) with an improved treatment of the earth rotation feedback (Mitrovica et al, 2005) (Section 1.5) to predict the global sea-level changes for each of our melt histories and 162 models of Earth structure (lithosphere thickness of 71, 96, and 120 km; upper mantle viscosity of 0.1, 0.2, 0.3, 0.5, 0.8, and 1 x 10^{21} Pas; and lower mantle viscosity of 1, 2, 3, 5, 8, 10, 20, 30, and 50 x 10^{21} Pas).

For each melt scenario, we calculate the resultant RSL at Barbados, Sunda Shelf, and Tahiti. Comparing these with the proxy evidence at the three sites, we constrain the MWP-1A source distribution by identifying the subset of the tested scenarios that satisfies the far-

field evidence, and determine the minimum and maximum contributions from each ice sheet group and the global MWP-1A source. These define our regional and global MWP-1A source constraints.

2.3.1 Justification of the Elastic Approach

The viscous response across MWP-1A at all three sites was calculated for the suite of model parameters described in Section 2.2.2 (324 model runs in total) (Fig 14), and determined to be small (< 1 m) compared to the amplitude of MWP-1A at each of the three far-field sites. Since it is small, we chose to treat only the elastic or static equilibrium "fingerprints" of the instantaneous gravitational-elastic-rotational response, which were calculated practically by applying an instantaneous melting event (Clark et al, 2002). The resultant sea-level fingerprint predictions then have the advantage of being insensitive to mantle viscosity structure, which is uncertain (Clark et al, 2002).

However, as an additional check on the effect of the viscous response, we also determine the MWP-1A source constraints when treating the viscous component as a second-order correction to the elastic fingerprints. Subtracting the second-order viscous correction from the far-field MWP-1A amplitude constraints, we get the elastic part of our far-field constraints, which we use to constrain our MWP-1A source distribution through a fingerprinting experiment. This approach which incorporates a viscous correction gives us MWP-1A source constraints that are identical to those obtained when the correction is not applied.

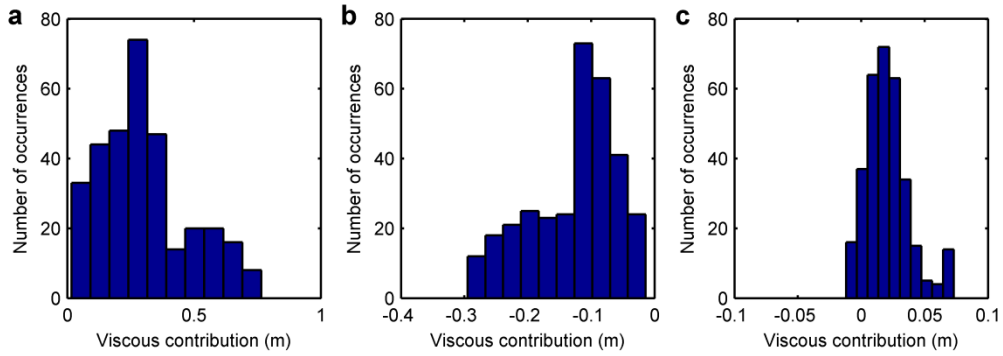

Figure 14: Histogram of viscous contributions to MWP-1A at Barbados (left), Sunda Shelf (centre), and Tahiti (right). All are small (< 1 m) compared to the MWP-1A amplitudes at the three far-field sites.

2.3.2 Results

First and foremost, what our results show is that, when we make our reassessments to the far-field data and consider our broader range of melting scenarios based on more recent deglaciation models, the far-field sea-level evidence and near-field geological constraints no longer contradict. When we test a suite of scenarios based on near-field models and evidence, against far-field constraints, we find that there exists quite a large subset of scenarios that satisfy both the near- and far-field evidence (Fig 15).

We find that instead of requiring a large (~15 m) AIS contribution to MWP-1A (Bassett et al, 2005), the far-field sea-level proxies allow for a wide range of MWP-1A source scenarios, ranging from those with zero Antarctic contribution to those with zero North American contribution (Fig 15c). Thus, the far-field sea-level constraints at Barbados (Fairbanks and Peltier, 2006), Sunda Shelf (Hanebuth et al, 2000), and Tahiti (Deschamps et al, 2012) are not as tight as previously thought (Clark et al, 2002; Bassett et al, 2005).

We can better constrain our results using NAIS contribution constraints from other studies. Using geological and modelling evidence, Carlson and Clark (2012) estimated that the NAIS contributed 4 to 6 m sea-level equivalent (sle) to MWP-1A for the 340-year period (solid black outline in Fig 15a and c). Taking this constraint for total NAIS contribution, the original far-field sea-level interpretations for Barbados (Peltier and Fairbanks, 2006) and

Sunda Shelf (Hanebuth et al, 2000) then require 4 to 10 m sle from the AIS, 0 to 2 m sle from the FIS, and 0 to 0.4 m sle from the GIS ice sheets, yielding a global sea-level rise of 12 to 16 m sle. By comparison, our revised interpretations allow for smaller AIS contributions, namely 1 to 10 m sle from the AIS, as well as 0 to 2 m sle from the FIS, and 0 to 0.4 m sle from the GIS, yielding a global sea-level rise of 9 to 14 m sle. This encompasses values for global MWP-1A amplitude that are considerably smaller than earlier estimates, which have ranged from 15 to 25 m sle (Peltier and Fairbanks, 2006; Clark et al, 2002), but is in agreement with the recent estimate from Tahiti of ~14 m sle (Deschamps et al, 2012).

Alternate interpretations of NAIS constraints yield different but compatible conclusions. For example, Tarasov et al (2012) estimate a NAIS contribution of 6 to 9 m sle for the 340-year period (dotted black outline in Fig 15a and 15c), which requires 0 to 7 m sle from the AIS, 0 to 2 m sle from the FIS, and 0 to 0.4 m sle from the GIS, yielding a global sea-level rise of 9 to 14 m sle (Table 2).

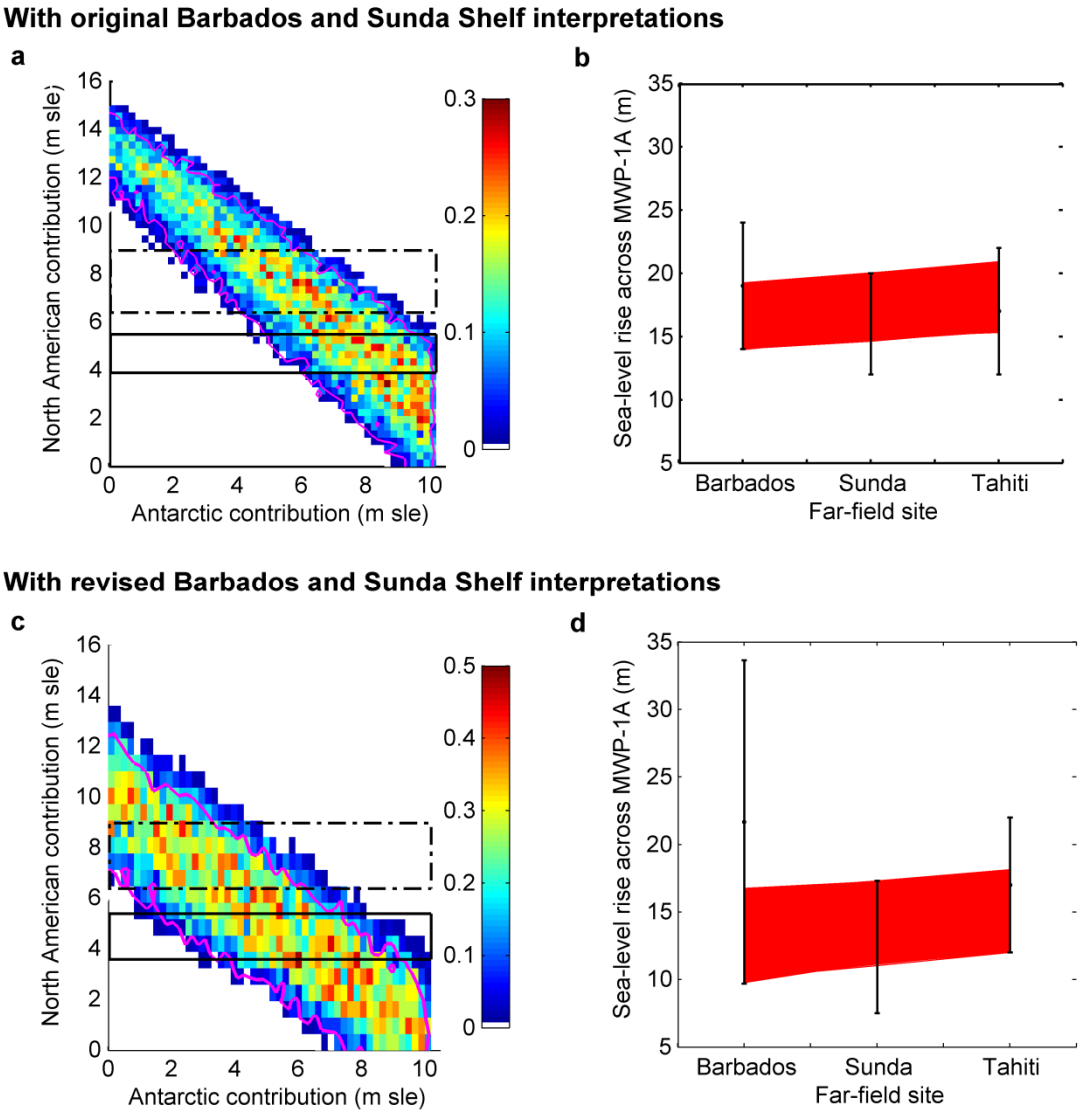

Figure 15: Distribution of melting scenarios that satisfy near- and far-field constraints using (a) previously-published (Peltier and Fairbanks, 2006; Hanebuth et al, 2000) and (c) revised Barbados and Sunda Shelf MWP-1A interpretations. In (a) and (c), the color scale denotes the density of melting scenarios that satisfy the far-field constraints, and the magenta contour shows the parameter space where 95% of these lie. The solid black outline highlights total contributions of 3.6-5.4 m sle from the NAIS estimated in a recent study (Carlson and Clark, 2012), while the dotted black outline shows the total NAIS contribution of 6.4-9.0 m sle, inferred by another recent study (Tarasov et al, 2012). In (b) and (d), vertical bars denote the MWP-1A amplitudes and uncertainties at each of the far-field sites, while red lines show the local MWP-1A amplitudes produced by scenarios that satisfy both the near-field and far-field constraints.

Table 2: Constraints on MWP-1A source partitioning

	MWP-1A contribution given NAIS constraints of	
	4 - 6 m sle[4]	**6 - 9 m sle[16]**
Antarctic ice sheets (AIS)	1 to 10 m sle	0 to 7 m sle
North American ice sheets (NAIS)	4 to 6 m sle	6 to 9 m sle
Fennoscandian ice sheet (FIS)	0 to 2 m sle	0 to 2 m sle
Greenland ice sheet (GIS)	0 to 0.4 m sle	0 to 0.4 m sle
TOTAL	9 to 14 m sle	9 to 14 m sle

2.3.3 Sensitivity to Spatial Function Type or Scaling Range Used

As mentioned in Sections 2.1.1 and 2.1.2, our results are insensitive to the type of spatial weighting functions used to define the AIS and NAIS melt in each scenario (Fig 16). That is to say, we get identical constraints on the MWP-1A source distribution when we repeat the fingerprinting experiment using only uniform spatial melting functions for AIS (Fig 7c and d; Fig 8) and NAIS (Fig 9c; Fig 10). Namely, using the total NAIS contribution constraints of 4 to 5 m sle from Carlson and Clark (2012), we get a global MWP-1A amplitude of 9 to 14 m, and 1 to 10 m from the AIS, 0 to 2 m sle from the FIS and 0 to 0.4 m from the GIS.

Likewise, as mentioned in Section 2.1.4, we get very similar results (Fig 17) when using a narrower range of AIS and NAIS melt contributions (scaling only between zero and the maximum melt contributions suggested in the source literature; Table 1, column 5). Specifically, when using the NAIS constraints of 4 to 6 m sle from Carlson and Clark (2012), we get a global MWP-1A amplitude of 9 to 11 m (compared with 9 to 14 m for the original choice of scaling range), with 2 to 5 m sle from the AIS (c.f. 1 to 10 m sle), 0 to 2 m sle from the FIS (c.f. 0 to 2 m sle), and 0 to 0.2 sle from the GIS (c.f. 0 to 0.4 m sle). The tighter constraints on AIS contribution and total MWP-1A amplitude are simply a result of our sampling, which does not consider AIS contributions of over 5 m. We prefer to use the broader scaling range (twice the maximum proposed in the relevant literature) since it helps

account for differences in the interpretation of near-field data (Carlson and Clark, 2012), and it is more consistent with the conservative nature of our analysis.

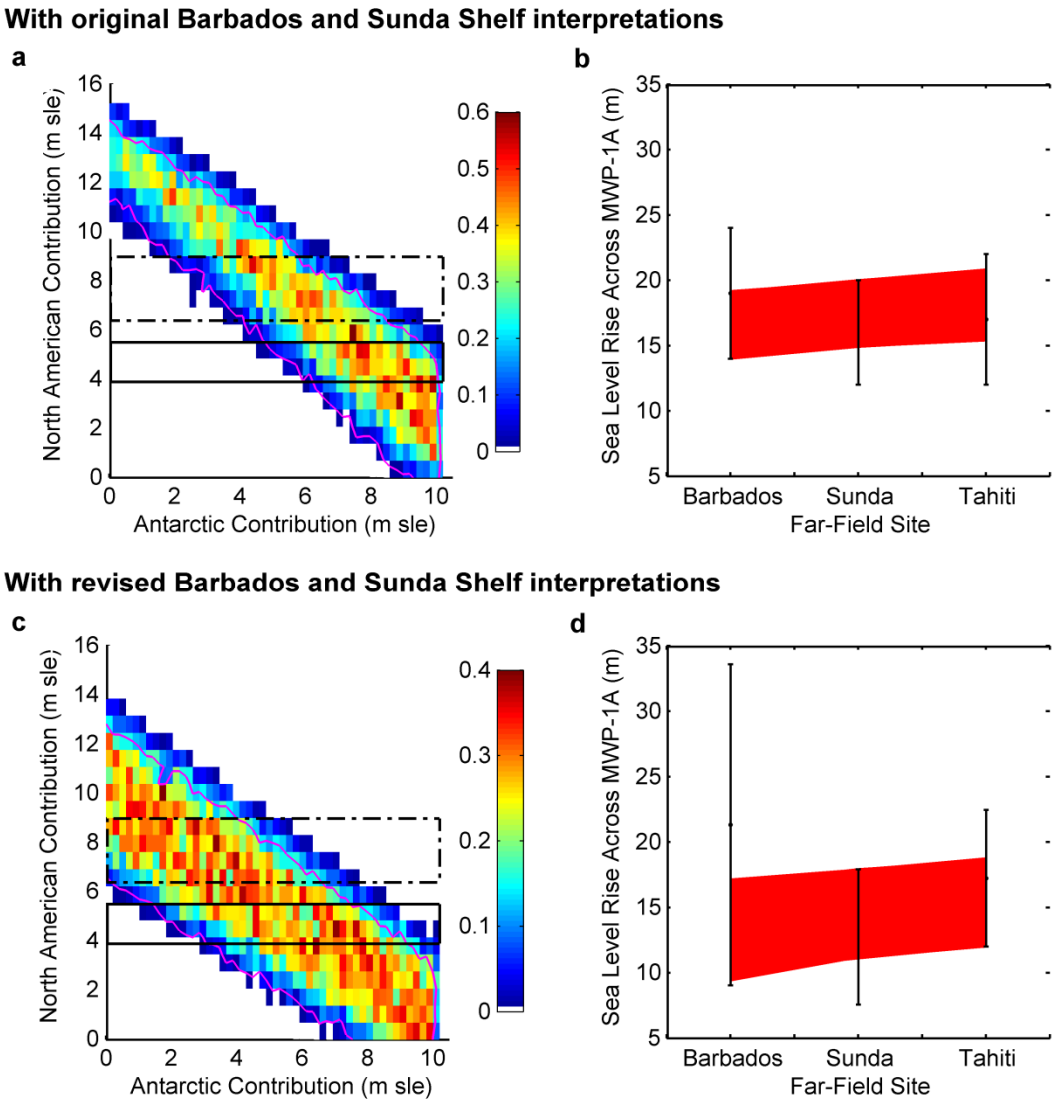

Figure 16: MWP-1A source distribution given uniform melting scenarios. Distribution of melting scenarios that satisfy near- and far-field constraints when using uniform melting scenarios described in Figs 7-10. Panels correspond with those in Fig 15.

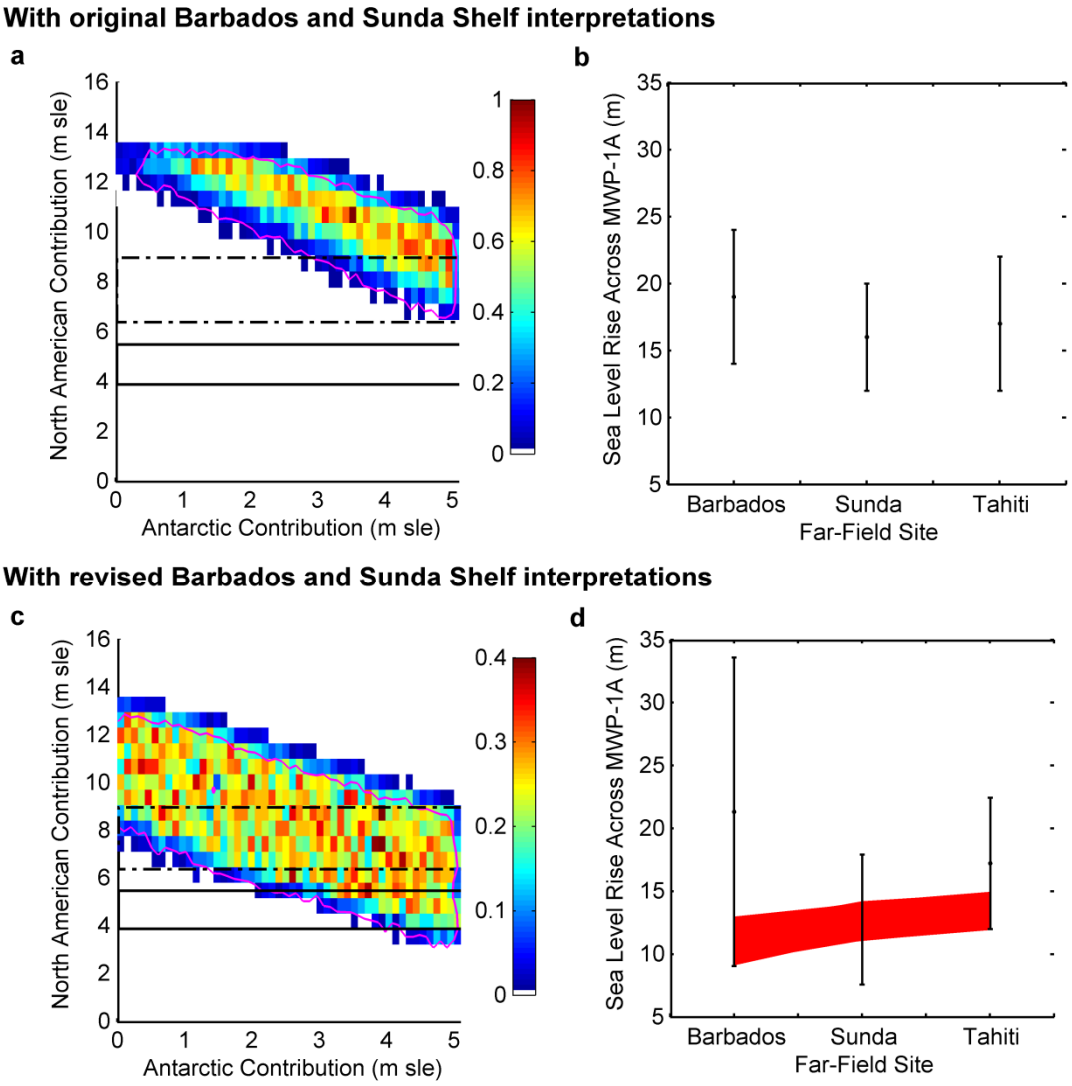

Figure 17: MWP-1A source distribution given narrower melt ranges. Distribution of melting scenarios that satisfy near- and far-field constraints when using narrower melt sampling ranges (Table 1, column 5). Panels correspond with those in Fig 15. Note that there are no scenarios that satisfy both the near-field and original far-field constraints.

2.3.4 Improved Local MWP-1A Amplitude Constraints

Treating the near- and far-field constraints jointly yields posterior estimates of the MWP-1A amplitude at each of the locations that are tighter than the observational constraints. Using the NAIS contribution estimate from Carlson and Clark (2012), the lower bounds on MWP-1A amplitude at Tahiti and Barbados, together with the upper bound at Sunda Shelf, leads to RSL constraints of 10-17 m at Barbados, 11-17 m at Sunda Shelf, and 12-18 m at Tahiti (Fig 15d).

2.3.5 Applying the "Most Probable" Tahiti MWP-1A Amplitude Range

Although Deschamps et al. (2012) defined the 12-22 m RSL range for MWP-1A at Tahiti as the broadest possible range, they also argued that a narrower "most probable" range is 14-18 m RSL. Applying this narrower far-field constraint together with the near-field constraint of 3.9 to 5.5 m sle for the total NAIS contribution (Carlson and Clark, 2012), we derive a posterior estimate for a total MWP-1A amplitude of 10 to 14 m sle (compared with 9 to 14 m sle) and AIS contribution of 3 to 10 m sle (compared with 1 to 10 m sle) (Fig 18).

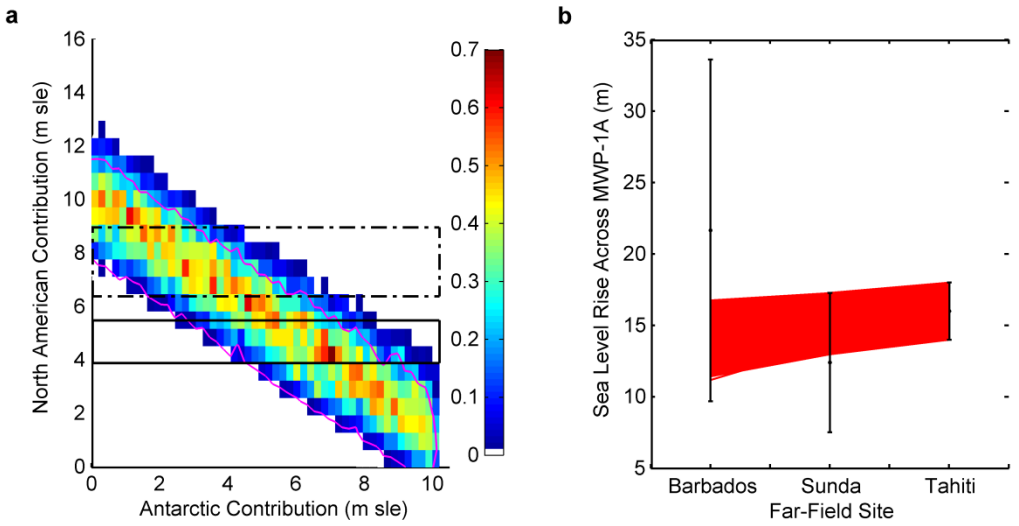

Figure 18: MWP-1A source distribution given narrower Tahiti constraints. Distribution of melting scenarios when using narrower far-field constraints of 14 to 18 m RSL at Tahiti (Deschamps et al, 2012). Panels correspond with those in Figure 15c and d.

2.4 Summary

Our reinterpretation of the amplitude of MWP-1A at Barbados and Sunda Shelf reconciles the apparent incompatibility of near- and far-field evidence by removing the constraint that the spatial variation in MWP-1A amplitude requires a large AIS contribution (Clark et al, 2002), although a large (~10 m) AIS contribution remains a possibility. Tighter constraints on partitioning the source of MWP-1A among the various ice sheets require new data from carefully selected locations, particularly from Antarctica (Carlson and Clark, 2012), as well as more precise constraints on the amplitude of MWP-1A at existing sites, with an emphasis on the lower bound at Barbados and Tahiti and the upper bound at Sunda Shelf (Fig 15d). So, while our results represent an important step towards better understanding the role of this event and the processes responsible for the highest recorded rates of sea-level change in Earth history, the far-field sea-level evidence at Barbados, Sunda Shelf, and Tahiti are, as of yet, unable to clearly distinguish between a large (up to ~10m) or small (near zero) contribution from the AIS.

Chapter 3
Improving MWP-1A Source Distribution Constraints through a Novel Near-Field Sea-level Data Approach

3.1 Incorporating Near-Field Sea-level Data

In this chapter, we explore a novel approach in which we incorporate data from a near-field sea-level site: Arisaig, Scotland (Shennan et al, 2000). Until now, sea-level constraints from near-field sites have been excluded from MWP-1A fingerprinting experiments because they are strongly influenced by local ice unloading. However, we overcome this by isolating the elastic component of the MWP-1A amplitude (i.e. fingerprint signal) at this location using a suite of models that provide optimum fits to the Scottish data. This removes near-field contamination and thereby makes the isolated elastic MWP-1A amplitude a suitable sea-level fingerprinting constraint. This can be used in conjunction with the intermediate- and far-field sites used in Chapter 2.

3.1.1 Arisaig, Scotland

The sea-level record at Arisaig (Shennan et al, 2000) is defined by microfossils found in sediment cores from isolation basins (Fig 19), which, due to the sea-level fall caused by post-glacial rebound (Section 1.5), become isolated from the open sea (Fig 20). In these environments, protection from high-energy waves, tides, and currents, by rock sills allow for the accumulation of sediments that are rich in microorganisms that have known livable ranges for factors like salinity or depth along an intertidal range (van de Plassche, 1986). This, along with lithostratigraphy and the radiocarbon dating of organic samples, can be used to reconstruct RSL histories for the local environment. This is specifically done by constraining the timings of marine isolation or connection events from the radiocarbon dating of microfossil samples and assigning them to altitude of the lowest part of the rock sill that separates the basin from the open sea (Shennan et al, 1994).

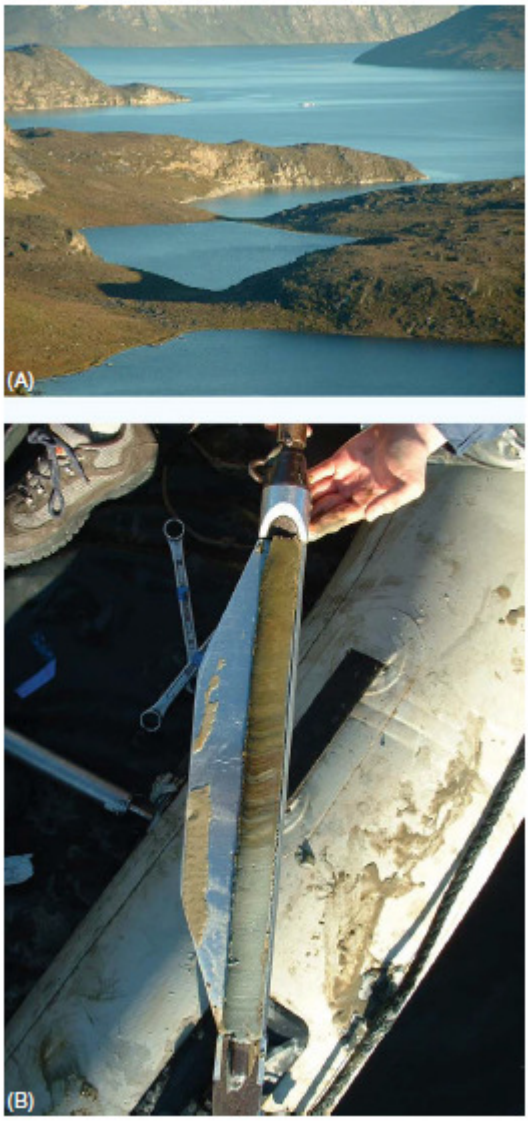

Figure 19: (a) Isolation basins in western Greenland with separating rock sills, and (b) a sediment core recovered from an isolation basin that shows an isolation sequence from gray, silty marine clay to brown, organic lake sediments. From Edwards (2007)

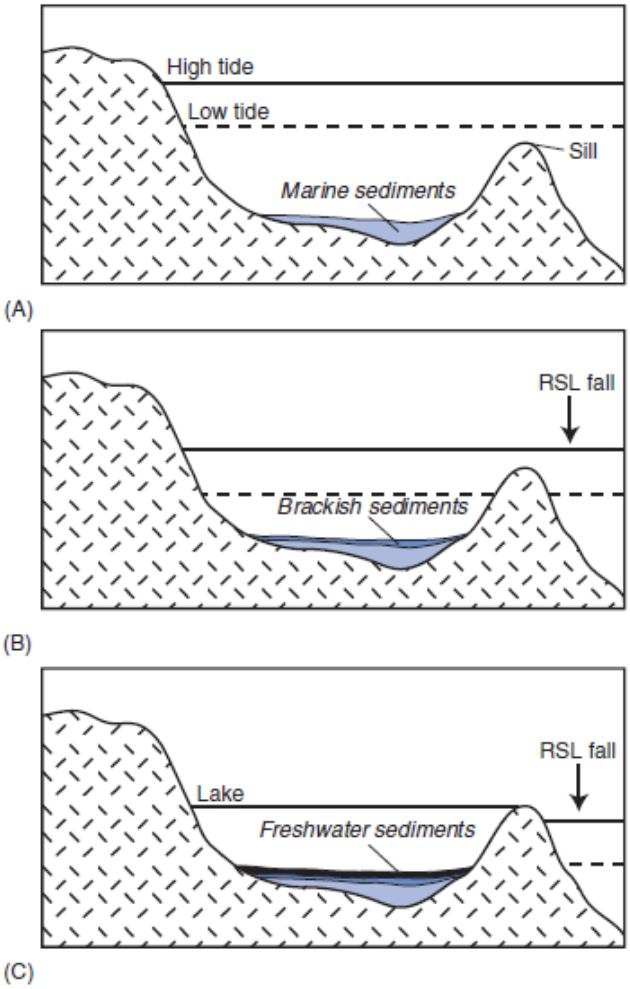

Figure 20: The isolation of a basin: (a) the basin is connected to the open sea, so marine sediments accumulate, (b) the sea-level falls and the basin is isolated from the open sea during low tides, so brackish sediments form, and (c) the basin is completely isolated from the open sea during high water, so freshwater sediments accumulate. From (Edwards, 2007).

The recalibrated (Reimer et al, 2009) ^{14}C record at Arisaig (Shennan et al, 2000) shows a fairly-linear decrease in RSL across the MWP-1A period, spanning from ~16 ka BP to 12 ka BP (Fig 25a). As mentioned previously, this signal is contaminated by near-field effects. The British-Irish ice sheet (BIIS) had, for the most part, fully-deglaciated by ~15 ka (Brooks et al, 2008; Hubbard et al, 2009); however, there is still a large viscous signal from the glacial isostatic rebound of the region (Clark et al, 1978) (Section 1.5). We will remove this viscous signal by applying a correction based on a subset of best-fit models from a

larger suite of 374 ice and earth model combinations. These include two alternate local models of the BIIS deglaciation (Brooks et al, 2008; Hubbard et al, 2009) pieced into two alternate global deglaciation models (Peltier, 2004; Bradley et al, 2011), for a total of four global ice models.

3.1.2 Local and Global Deglaciation Models

We use two alternate deglaciation models for the BIIS: the Brooks et al (2008) model and the Hubbard et al (2009) E102b2 reconstruction (Fig 21 and 22). The Brooks et al (2008) model is constructed from a database of local RSL observations and geophysical models that calculate RSL change due ice sheet growth or ablation, while the Hubbard et al (2009) E102b2 reconstruction uses a 3D thermomechanical model with surface mass balance driven by a reference climatology and tested for consistency with the local ice-directional record from the BRITICE Geographical Information System (Clark et al, 2004) and local RSL history (Shennan et al, 2005).

In order to generate RSL predictions, local BIIS deglaciation models must be pieced into a global ice model. Following Bradley et al (2011) and Kuchar et al (2012), we piece the Brooks et al (2011) and E102b2 (Hubbard et al, 2009) BIIS models, respectively, into the global model of Bradley et al (2011). In addition to this, for a more conservative approach, we also consider the BIIS ice models pieced into a very different global model, ICE5G (Peltier, 2004). While the Bradley et al (2011) model, based on the Bassett et al (2005) model, assumes a large (~ 15 m sle) contribution to MWP-1A from the Antarctic, ICE5G include no significant Antarctic melt for that time period. This gives us a good variety in global ice models considered.

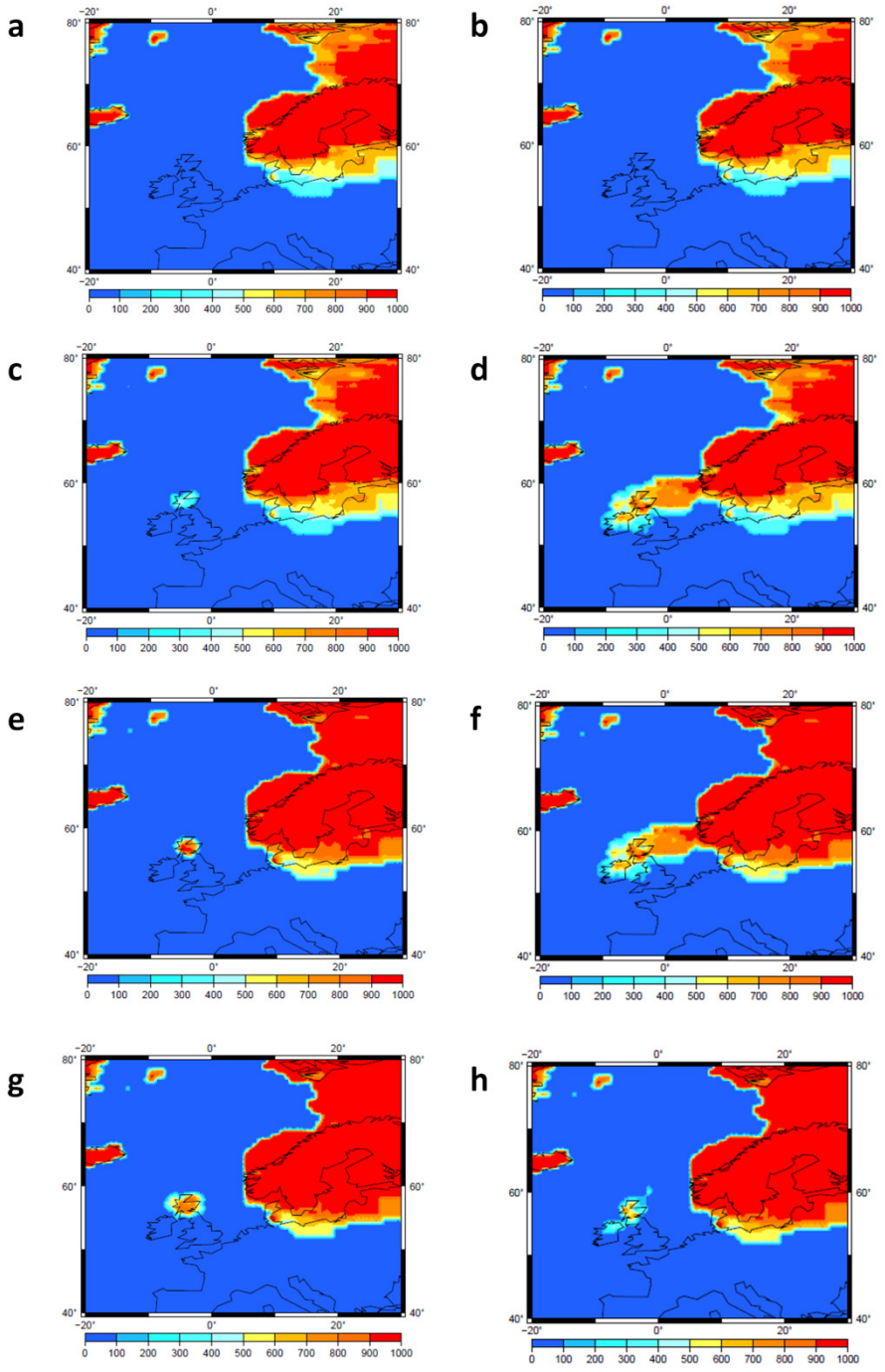

Figure 21: BROOKS_5G (left column) and HUBMIN_5G (right column) deglaciation models at times: 46 ka (a, b), 32 ka (c,d), 27 ka (e,f), and 26 ka (g,h).

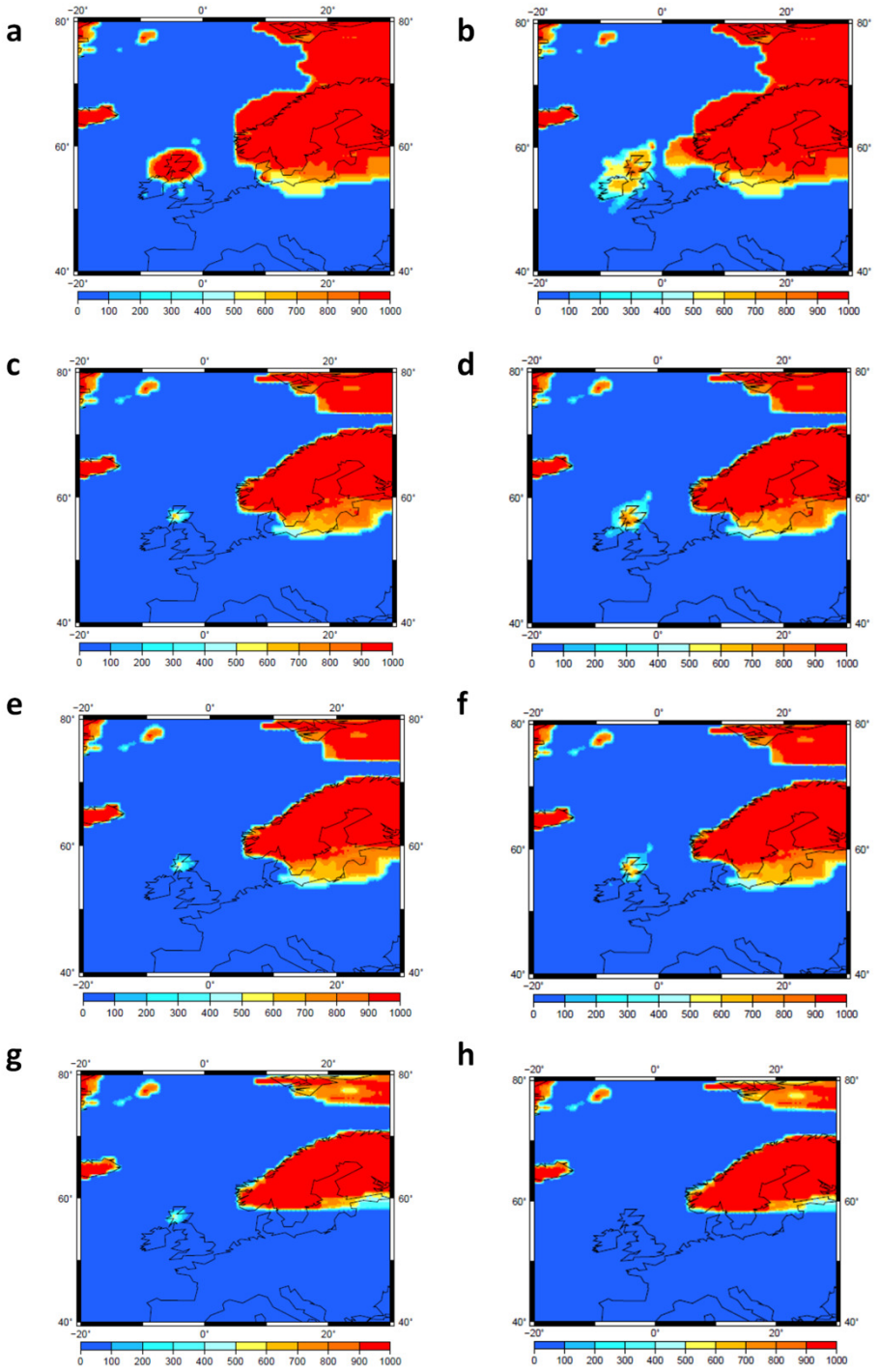

Figure 22: BROOKS_5G (left column) and HUBMIN_5G (right column) deglaciation models at times: 24 ka (a, b), 17 ka (c,d), 16 ka (e,f), and 15 ka (g,h).

For simplicity, we will refer to the four composite ice models as: BROOKS_5G, BROOKS_SLB, HUBMIN_5G, and HUBMIN_SLB. Their associated local and global source models are listed in Table 3.

Table 3: Composite ice models used for Arisaig viscous correction.

	Local Ice Model	**Global Ice Model**
BROOKS_5G	Brooks et al (2008)	ICE5G (Peltier et al, 2004)
BROOKS_SLB	Brooks et al (2008)	Bradley et al (2011)
HUBMIN_5G	E102b2 (Hubbard et al, 2009)	ICE5G (Peltier et al, 2004)
HUBMIN_SLB	E102b2 (Hubbard et al, 2009)	Bradley et al (2011)

3.1.3 Determining Best-Fit Ice and Earth Model Combinations

We identify a subset of ice and earth model combinations that provide best fit to sea-level observations at Arisaig (Shennan et al, 2000) and two other locations in northwestern Scotland with records spanning the MWP-1A period, namely Kentra and Knapdale (Shennan et al, 2000). For each of the four composite ice models, we vary the upper and lower mantle viscosity structure and calculate the χ^2 misfit between the sea-levels predicted using the Kendall et al (2005) sea-level algorithm and Mitrovica et al (2005) treatment of earth rotation feedback, and those observed. Because of the large age uncertainties in the Scottish sea-level data (Shennan et al, 2000), we incorporate age uncertainties in our χ^2 statistic as follows:

$$\chi 2 = \frac{1}{\mathrm{N}} \sum_{\mathrm{i}=1}^{\mathrm{N}} \frac{\mathrm{s}_{\mathrm{i}}^{\mathrm{pred}} - \mathrm{s}_{\mathrm{i}}^{\mathrm{obs}}}{\sigma_{\mathrm{i}}^{\mathrm{tot}}} \tag{5}$$

where

$$\sigma_i^{tot} = \sigma_i + m_i^{pred} dt_i^{obs} \tag{6}$$

and s_i^{pred} and s_i^{obs} are the predicted and observed sea-levels at time i, respectively. σ_i^{tot} is the total time error on the observed sea-level point, defined as the sum of the uncertainty in the relative sea-level observation and the product of the instantaneous slope on the predicted sea-level curve and the age uncertainty of the observation.

Previous studies (Bradley et al, 2011; Kucher et al, 2012) have found that the BROOKS_SLB and HUBMIN_SLB models best fit sea-level data across the British Isles region when using a lithosphere thickness of 71 km (with significant decreases in the quality of fit for thicknesses of 96 km or 120 km). As such, in this analysis, we will consider only a lithosphere of 71 km thickness.

We find that the BROOKS_SLB and BROOKS_5G models (with minimum χ^2 values of 1.6 and 1.7) fit the Scottish sea-level data from northwest Scotland (Arisaig, Kentra, and Knapdale) significantly better than the HUBMIN_SLB or HUBMIN_5G models (with minimum χ^2 values of 3.2 and 3.6) (Fig 23). The best-fit subset of ice and earth model combinations (BROOKS_SLB and BROOKS_5G with lithosphere thickness of 71 km, upper mantle viscosity of 0.2 to 0.3 x 10^{21} Pa s, and lower mantle viscosity of 1 to 90 x 10^{21} Pa s; and ice model BROOKS_SLB with lithosphere thickness of 71 km, upper mantle viscosity of 0.5 x 10^{21} Pa s, and lower mantle viscosity of 2 to 8 x 10^{21} Pa s or 10 to 90 x 10^{21} Pa s), defined as those that are within 95% confidence of the optimum ice and earth model (BROOKS_5G, lithosphere thickness of 71 km, upper mantle viscosity of 0.2 x 10^{21} Pa s, and lower mantle viscosity of 20 x 10^{21} Pa s), is outlined by the magenta contours. None of the HUBMIN_SLB or HUBMIN_5G models satisfy the 95% confidence χ2 cut-off.

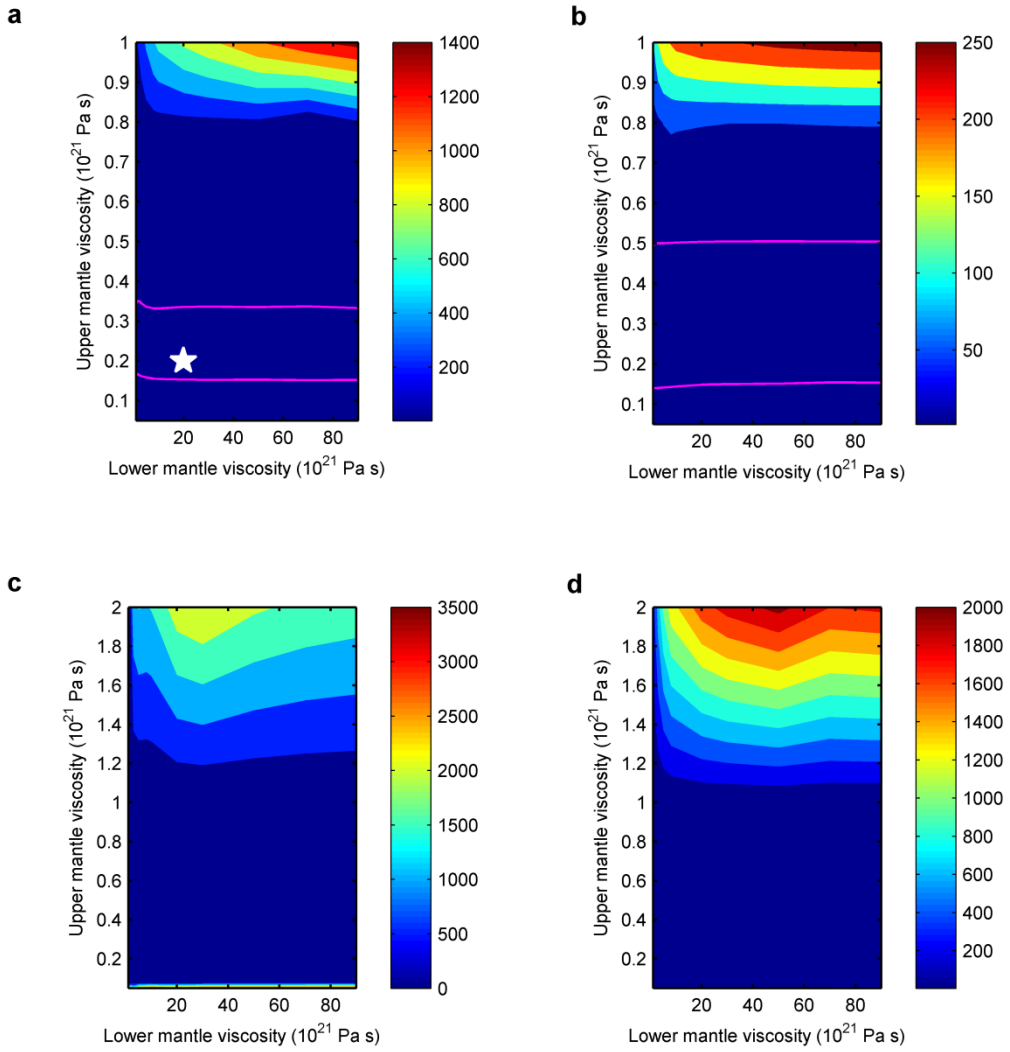

Figure 23: Contour plots of the χ^2 misfit between predicted and observed sea-levels in northwest Scotland as a function of upper and lower mantle viscosity for a lithosphere thickness of 71 km and ice models: (a) BROOKS_5G, (b) BROOKS_SLB, (c) HUBMIN_5G, and (d) HUBMIN_SLB. The white star in subplot (a) indicates the optimum earth model, while the magenta contours identify the suite of 31 best-fit models (95% confidence).

3.1.4 Isolating the Elastic MWP-1A Amplitude

We then isolate the elastic MWP-1A amplitude by calculating a correction and uncertainty based on the above-calculated subset of best-fit models. For each of the 31 best-fit ice and earth model combinations, using the sea-level algorithm of Kendall et al (2005) and Mitrovica et al (2005) treatment of the earth rotation feedback (Section 1.5), we calculate three particular components of the glacial isostatic adjustment (GIA) signal at Arisaig, which will then be removed from the local sea-level record to isolate the elastic part of the signal.

The first component of the correction is the removal of the viscous response due to ice, ocean, and rotation loading changes prior to MWP-1A from the sea-level records during and immediately-after MWP-1A (Fig 24a). These include the indirect gravitational effect and the solid earth response to ice-ocean mass loading redistribution (Section 1.5). Because of the long timescale of mantle flow and solid earth adjustment, the viscous response to a loading event can continue for many thousands of years after it has ended. In fact, the solid earth is still responding today to loading changes from the Last Deglaciation (Simons and Hager, 1997).

The second component of the correction, similar to the first, is the removal of the viscous response due to loading changes during MWP-1A from the sea-level record after MWP-1A (Fig 24b).

The third component of the correction, however, is a little different; it is the removal of the total response (viscous, elastic, direct, and eustatic) (Section 1.5) due to loading changes after MWP-1A (Fig 24c). This is done because there are no local data constraints immediately at the end of the pulse (~14.3 ka). So, to constrain the local sea-level at the end of the pulse, we must use the sea-level evidence from between roughly 13 and 12 ka BP (Fig 25). These are influenced by post-MWP-1A melting, however, by subtracting the total response due to melting after MWP-1A, we shift the data constraints so that they effectively express the local sea-level at the end of the pulse.

The sum of these three corrections is our total correction for each ice and earth model combination (Fig 24d). Removing the viscous components in corrections (1) to (2) corrects the near-field contamination caused by the GIA response to unloading near recently-deglaciated or deglaciating ice sheets, while correction (3) effectively migrates data post-MWP-1A data points to the end of the MWP-1A period.

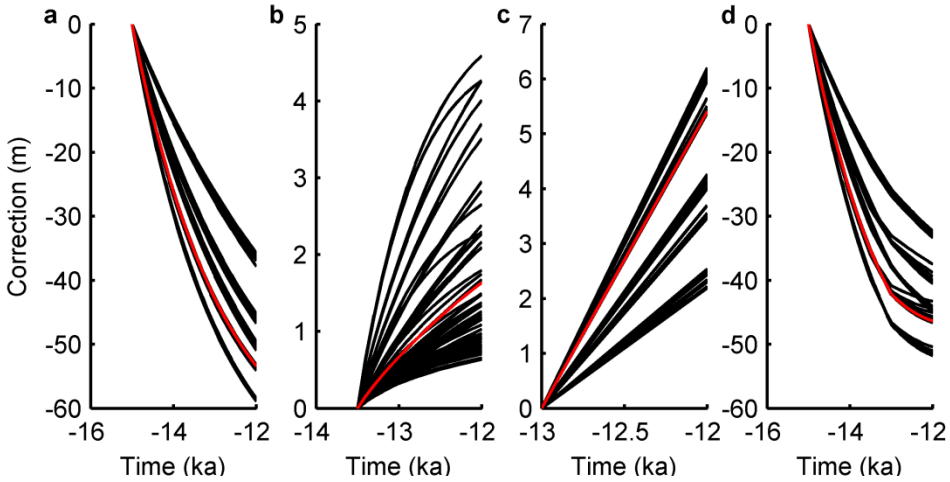

Figure 24: Viscous corrections to the Arisaig sea-level data corresponding to (a) viscous response due to loading changes prior to MWP-1A, (b) the viscous response due to loading changes across MWP-1A, and (c) the total response due to loading after MWP-1A. Corrections are in red for the sample model (ice model BROOKS_5G, lithosphere thickness of 71 km, upper mantle viscosity of 0.2 x 10^{21} Pa s, and lower mantle viscosity of 20 x 10^{21} Pa s), and in black for all others. The total correction for this sample model is plotted in (d).

We find that, at Arisaig, it is the viscous component of sea-level rise due to pre-MWP-1A load changes (Fig 24a) that dominates the local correction (Fig 24d). There is quite a bit of uncertainty associated with all three components of the sea-level correction. Defining our correction uncertainty using the variance between the various models, we apply the correction and find that it constrains the local elastic MWP-1A amplitude at Arisaig to between 11 and 42 m (Fig 25). However, it is important to note that it is only improvements to the lower bound of this range that is important for further constraining the source distribution of MWP-1A (Fig 26).

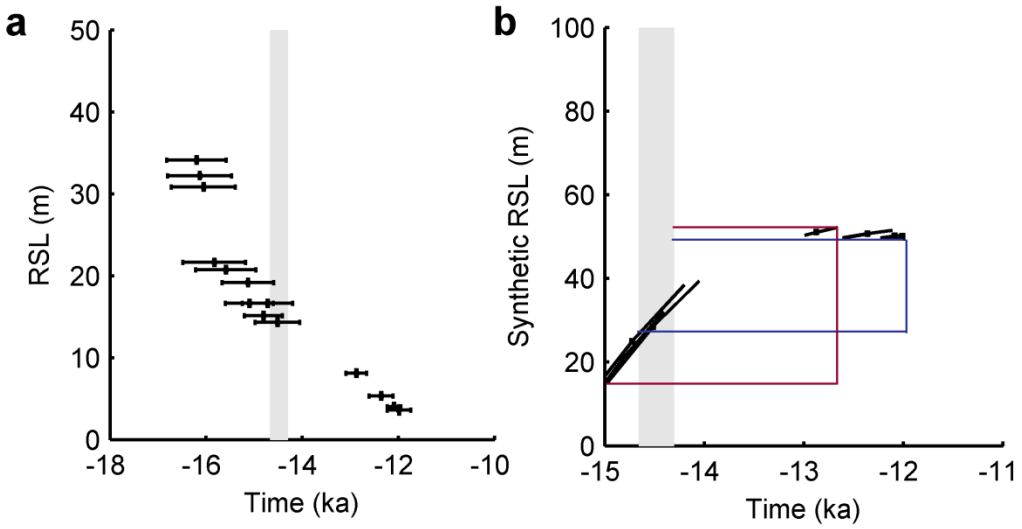

Figure 25: Application of the viscous correction associated with sample model (BROOKS_5G, lithosphere thickness of 71 km, upper mantle viscosity of 0.2 x 10^{21} Pa s, and lower mantle viscosity of 20 x 10^{21} Pa s). Subplot (a) shows the raw sea-level data from Arisaig, while (b) shows just the elastic part. In (a), horizontal bars denote age uncertainty while vertical bars denote RSL uncertainty. In (b), the vertical bars denote the RSL measurement uncertainty, while diagonal bars denote the RSL uncertainty associated with the age uncertainty and correction. The red and blue lines show how the maximum and minimum elastic MWP-1A amplitudes are defined for this particular ice and earth model combination. The final MWP-1A amplitude constraints of 11 to 42 m at Arisaig are the minimum and maximum MWP-1A amplitudes determined across the full suite model combinations.

3.2 Sea-Level Fingerprinting Results

We repeat the sea-level fingerprinting experiment in Section 2.3.2, including our Arisaig elastic MWP-1A amplitude as an additional sea-level constraint. We find that this leads to an improved MWP-1A source distribution constraint than when using the intermediate- and far-field data alone (Fig 26; Table 4). Using the Carlson and Clark (2012) constraints of 4 to 6 m from the NAIS, we find that the sea-level constraints at Arisaig, Barbados, Sunda Shelf, and Tahiti require a MWP-1A source contribution of 5 to 10 m sle from the AIS, 0 to 2 m sle from the FIS, and 0 to 0.4 m sle from the GIS, yielding a global sea-level rise of 11 to 14 m sle. We get a similar tightening of the source constraints when using the Tarasov et al (2012) interpretation of 6 to 9 m from the NAIS (Table 4).

Table 4: Constraints on MWP-1A source partition when including or excluding the elastic Arisaig MWP-1A constraint

	Given NAIS constraints of 4 - 6 m sle (Carlson and Clark, 2012)		**Given NAIS constraints of 6 to 9 m sle (Tarasov et al, 2012)**	
	Without Arisaig Constraint	**With Arisaig Constraint**	**Without Arisaig Constraint**	**With Arisaig Constraint**
Antarctic ice sheets (AIS)	1 to 10 m sle	5 to 10 m sle	0 to 7 m sle	2 to 7 m sle
North American ice sheets (NAIS)	4 to 6 m sle	4 to 6 m sle	6 to 9 m sle	6 to 9 m sle
Fennoscandian ice sheet (FIS)	0 to 2 m sle	0 to 2 m sle	0 to 2 m sle	0 to 2 m sle
Greenland ice sheet (GIS)	0 to 0.4 m sle	0 to 0.4 m sle	0 to 0.4 m sle	0 to 0.4 m sle
TOTAL	9 to 14 m sle	11 to 14 m sle	9 to 14 m sle	11 to 14 m sle

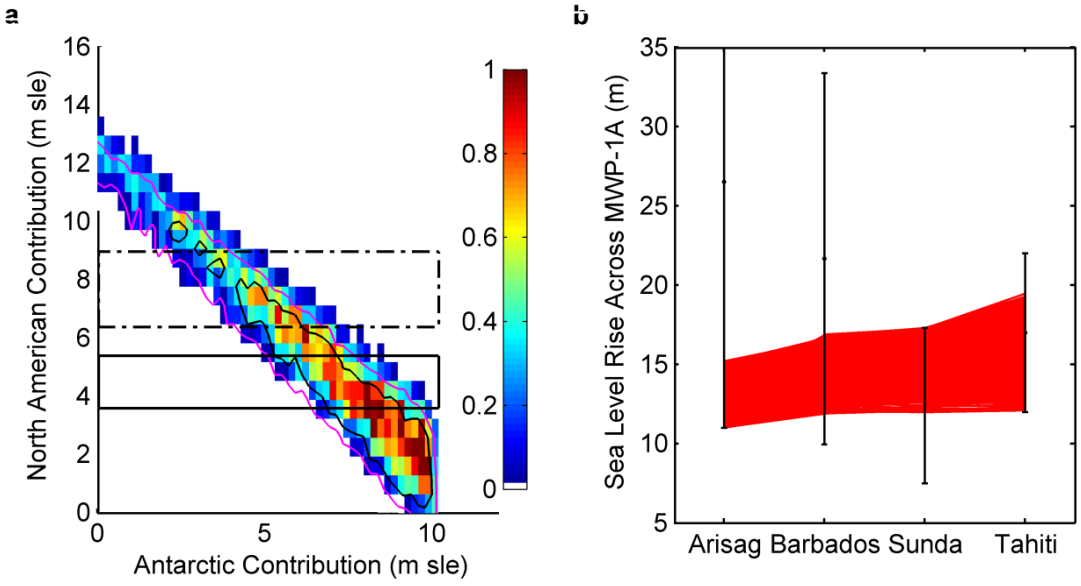

Figure 26: MWP-1A source distribution when including the elastic Arisaig constraint. Panels correspond to those in Fig 15c and d. The black contour in (a) corresponds to 1-sigma confidence.

Including the Arisaig sea-level constraint excludes AIS contributions of less than 2 m sle and favours larger global MWP-1A amplitudes (Table 4). Taking the union of the Clark et al (2012) and Tarasov et al (2012) NAIS constraints, we get a MWP-1A source distribution of 2 to 10 m sle from the AIS, 4 to 9 m sle from the NAIS, 0 to 2 m sle from the FIS, and 0 to 0.4 m sle from the GIS, yielding a global MWP-1A amplitude of between 9 and 14 m sle.

In addition to this, we find that the near-field constraints that define the melting scenarios and the far-field constraints at Sunda the Shelf and Tahiti lead to tighter constraints on the elastic MWP-1A amplitude at Arisaig (Fig 26b). In comparison to the 11 to 42 m constraint from observational evidence and correction uncertainties, the sea-level fingerprinting exercise constrains the elastic MWP-1A amplitude to just between 11 and 15 m at Arisaig.

Though the constraint on the AIS contribution remains broad, it is important to note that there is a strong dependence on the NAIS contribution. This means that the tightening of the NAIS constraint, or for example, the exclusion of either one of the NAIS interpretations, will result in a significant improvement to the AIS constraint. Moreover, analogous to what we found in Chapter 2, more precise constraints on the lower bound of the elastic MWP-1A amplitude at Arisaig can also lead to tighter constraints on the source distribution (Fig 26b).

3.3 Summary

In this experiment, we have demonstrated how constraints from a near-field sea-level site can be included in an elastic fingerprinting experiment, specifically to constrain the source distribution of MWP-1A.Though the constraint at Arisaig, Scotland, the particular location we chose, cannot distinguish between a small (2-3 m sle) or large (up to 10 m) AIS source, it does improve the source distribution constraint by excluding insignificant AIS contributions (of less than 2 m). This is consistent with recent studies by Carlson and Clark

(2012) and Weber et al (2013) that suggest a significant AIS contribution, though neither study can confidently quantify it.

Moreover, this exercise is important because it paves the way for the future inclusion of other near-field sea-level constraints. The correction method applied at Arisaig can be repeated for other near-field sites in the British Isles region as well as possibly elsewhere in the Northern and Southern Hemispheres. Perhaps the inclusion of other near-field constraints will lead to an even tighter constraint of the AIS contribution to MWP-1A. This will lead to better models of past deglaciation and well as a basis for further understanding of past ice sheet dynamics and events of rapid sea-level rise, which will be of interest in constraining future rates of sea-level rise.

Chapter 4
Conclusion

4.1 Summary of Key Results

In this study, we show that the incorporation of updated melting scenarios, as well as our reassessments of the sea-level data at Barbados (Fairbanks and Peltier, 2006) and Sunda Shelf (Hanebuth et al, 2000) and the new sea-level evidence from Tahiti (Deschamps et al, 2012) results in a reconciliation of the near- and far-field evidence, regarding the source distribution of MWP-1A. Namely, we demonstrate that the geophysical constraints from sea-level fingerprinting, which, until now, have been the primary source of evidence of a large Antarctic source (Clark et al, 2002; Bassett et al, 2005) no longer require a large (~15 m sle) AIS contribution. Instead, we find that the AIS could have contributed as little as 2 m sle, or as much as 10 m sle (Section 3.2).

We also constrain the total (eustatic) MWP-1A amplitude to 11 to 14 m sle (Section 3.2) by considering the constraints from Arisaig, in addition to our intermediate- and far-field sites Barbados, Sunda Shelf, and Tahiti. This compares with a eustatic MWP-1A amplitude prediction of 9 to 14 m sle when considering only the intermediate- and far-field sites (Section 2.3.2) and predictions from previous studies of 14 to 25 m sle (Clark et al, 2002; Bassett et al, 2005; Deschamps et al, 2012).

We also demonstrate how near-field sea-level evidence can be incorporated into static equilibrium sea-level fingerprinting experiments, through the example of Arisaig, Scotland (Shennan, 2000) (Chapter 3). This is a novel technique which can be further applied to sea-level data from sites located close to formerly-glaciated regions. We show that the inclusion of the sea-level evidence at Arisaig improves the constraint of MWP-1A source distribution, and while the constraint remains broad, our study identifies a number of avenues for future work.

4.2 Next Steps

In previous sections, we have already highlighted a number of ways through which the source distribution of MWP-1A can be better constrained, many of which involved placing tighter constraints on either the local sea-level records or deglaciation models. These would involve the reassessment of existing data and/or the collection or more evidence. Many funded projects are underway including a recent IODP expedition (Great Barrier Reef Expedition 325). Provided that the core samples capture the local sea-level chronology across the timing of MWP-1A, this can provide an additional intermediate- to far-field constraint in a sea-level fingerprinting experiment.

Our methodology for incorporating near-field sea-level evidence (Chapter 3) can also be applied to records from other near-field locations, i.e. Andoya (Lambeck et al, 1998), however the effectiveness of this approach is dependent on how well the local sea-level at those sites is constrained. A next step would be to examine available far-field sea-level records and determine their suitability with respect to this technique.

References

Ackert, R.P., Mukhopadhyay, S., Parizek, B.R. & Borns, H.W. Ice elevation near the West Antarctic Ice Sheet divide during the Last Glaciation. *Geophys. Res. Lett.* **34,** L21506 (2007).

Bard, E., Hamelin, B. & Fairbanks, R.G. U-Th ages obtained by mass spectrometry in corals from Barbados: Sea-level during the past 130,000 years. *Nature* **346**, 456-458 (1990).

Bard, E. *et al*. Deglacial sea-level record from Tahiti corals and the timing of global meltwater discharge. *Nature* **382**, 241-244 (1996).

Bassett, S.E., Milne, G.A., Mitrovica, J.X. & Clark, P.U. Ice sheet and solid earth influences on far-field sea-level histories. *Science* **309,** 925-928 (2005).

Bradley, S.L., Milne, G.A., Shennan, I., & Edwards, Robin. An improved Glacial Isostatic Adjustment model for the British Isles. *J. Quat. Sci.* **26**(5), 541-552 (2011).

Broecker, W.S. The biggest chill. *Natural History* **96**(10), 74-82 (1987).

Brooks, A.J. *et al*. Postglacial relative sea-level observations from Ireland and their role in glacial rebound modelling. *J. Quat. Sci.* **23**(2), 175-192 (2008).

Carlson, A.E. *et al*. Modeling the surface mass-balance response of the Laurentide Ice Sheet to Bølling warming and its contribution to Meltwater Pulse 1A. *Earth Planet. Sci. Lett.* **315-316,** 24-29 (2012).

Carlson, A.E. & Clark, P.U. Ice sheet sources of sea-level rise and freshwater discharge during the last deglaciation. *Rev. Geophys.* **50,** RG4007 (2012).

Chappell, J. & Polach, H. Post-glacial sea-level rise from a coral record at Huon Peninsula, Papua New Guinea. *Nature* **349**, 147-149 (1991).

Charles, C.D. & Fairbanks, R.D. Evidence from Southern Ocean sediments for the effect of North Atlantic deep-water flux on climate. *Nature* **355**, 416-419 (1992).

Clague, J.J. & James, T.S. History and isostatic effects of the last ice sheet in southern British Columbia. *Quat. Sci. Rev.* **21**(1-3), 71-87 (2002).

Clark, C.D. *et al*. Map and GIS database of glacial landforms and features related to the last British Ice Sheet. *Boreas* **33**(4), 359-375 (2004).

Clark, J.A., Farrell, W.E., & Peltier, W.R. Global Changes in Postglacial Sea-level: A Numerical Calculation. *Quat Res*. **9**, 265-287 (1978).

Clark, P.U., Mitrovica, J.X., Milne, G.A. & Tamisiea, M.E. Sea-level fingerprinting as a direct test for the source of global meltwater pulse 1A. *Science* **295,** 2438-2441 (2002).

Cutler, K.B. *et al*. Rapid sea-level fall and deep-ocean temperature change since the last interglacial period. *Earth Planet. Sci. Lett.* **206**(3-4), 253-271 (2003).

Deschamps, P. *et al.* Ice-sheet collapse and sea-level rise at the Bolling warming 14,600 years ago. *Nature* **483,** 559-564 (2012).

Edwards, R.L. Paleotopography of glacial-age ice sheets. *Science* **267**(5197), 536-538 (1995).

Fairbanks, R.G. A 17,000-year glacio-eustatic sea-level record: influence of glacial melting rates on the Younger Dryas event and deep-ocean circulation. *Nature* **342**, 637-642 (1989).

Farrell, W.E. & Clark, J.A. On Postglacial Sea-level. *Geophys. J. Int.* **46**(3), 647-667 (1976).

Gregoire, L.J., Payne, A.J. & Valdes, P.J. Deglacial rapid sea-level rises caused by ice-sheet saddle collapses. *Nature* **487,** 219-222 (2012).

Hanebuth, T., Stattegger, K. & Grootes, P.M. Rapid flooding of the Sunda shelf: a late-glacial sea-level record. *Science* **288,** 1033-1035 (2000).

He, F. *Simulating Transient Climate Evolution of the Last deglaciation with CCSM3*.PhD Thesis: University of Wisconsin-Madison: USA (2010).

Hubbard, A. *et al*. Dynamic cycles, ice streams and their impact on the extent, chronology and deglaciation of the British-Irish ice sheet. *Quat. Sci. Rev.* **28**, 758-776 (2009).

Kendall, R.A., Mitrovica, J.X. & Milne, G.A. On post-glacial sea-level – II. Numerical formulation and comparative results on spherically symmetric models. *Geophys. J. Int.* **161,** 679-706 (2005).

Kuchar, J. *et al*. Evaluation of a numerical model of the British-Irish ice sheet using relative sea-level data: implications for the interpretation of trim line observations. *J. Quat. Sci.* **27**(6), 597-605 (2012).

Lambeck, K. Smither, C. & Johnston, P. Sea-level change, glacial rebound and mantle viscosity for northern Europe. *Geophys. J. Int.* **134,** 102-144 (1998).

Lambeck, K., Yokoyama, Y. & Purcell, T. Into and out of the Last Glacial Maximum: sea-level change during Oxygen Isotope Stages 3 and 2. *Quat. Sci. Rev.* **21,** 343-360 (2002).

Lehman, S.J. & Keigwin, L.D. Deep circulation revisited. *Nature* **358**, 197-198 (1992).

Lighty, R.G. Fleshy-algal domination of a modern Bahamian barrier reef: example of an alternate climate reef community. *Proc. 4th Int. Coral Reef Symp. Manila* **1,** 772 (1981).

Mackintosh, A. *et al*. Retreat of the East Antarctic ice sheet during the last glacial termination. *Nat. Geosci.***4,** 195-202 (2011).

Milne, G. & Shennan I. Sea Level Studies | Isostasy: Glaciation-Induced Sea-Level Change. *Encyclopedia of Quaternary Science (2ed)*, Ed: S.A. Elias, Amsterdam, 452-459 (2013).

Mitrovica, J.X., Tamisiea, M.E., Davis, J.L., & Milne, G.A. Recent mass balance of polar ice sheets inferred from patterns of global sea-level change. *Nature* **409**(6823), 1026-1029 (2001).

Mitrovica, J.X. & Milne, G.A. On the origin of late Holocene sea-level highstands within equatorial basins. *Quat. Sci. Rev.* **21**(20-22), 2179-2190 (2002).

Mitrovica, J.X., Wahr, J., Matsuyama, I. & Paulson, A. The rotational stability of an ice-age earth. *Geophys. J. Int.* **161,** 491-506 (2005).

Neumann, A.C., & McIntyre, I.G. Reef response to sea-level rise: Keep-up, catch-up, or give-up. *Proc. 5th Int. Coral Reef Cong. Tahiti* **3,** 105-110 (1985).

Peltier, W.R. Ice age paleotopography. *Science* **273**, 195-201 (1994).

Peltier, W.R. Paleotopography of glacial-age ice sheets: Reply. *Science* **267**(5197), 536-538 (1995).

Peltier, W.R. On eustatic sea-level history: Last Glacial Maximum to Holocene. *Quat. Sci.Rev.* **21**(1-3), 377-396 (2002).

Peltier, W.R. Global glacial isostasy and the surface of the ice-age Earth: the ice-5G (VM2) model and GRACE. *Annu. Rev. Earth Planet Sci.* **32,** 111-149 (2004).

Peltier, W.R. On the hemispheric origins of meltwater pulse 1a. *Quat. Sci. Rev.* **24**(14-15), 1655-1671 (2005).

Peltier, W.R. & Fairbanks, R.G. Global glacial ice volume and Last Glacial Maximum duration from an extended Barbados sea-level record. *Quat. Sci. Rev.* **25,** 3322-3337 (2006).

Reimer, P.J. *et al*. Intcal09 and Marine09 radiocarbon age calibration curves, 0-50,000 years cal BP. *Radiocarbon* **51,** 1111-1150 (2009).

Shennan, I., Innes, J.B., Long, A.J., & Zong, Y. Late Devensian and Holocene relative sea-level changes at Lock nan Eala, near Arisaig, northwest Scotland. *J. Quat. Sci.* **9**(3), 261-283 (1994).

Shennan, I. *et al*. Late Devensian and Holocene records of relative sea-level changes in northwest Scotland and their implications for glacio-hydro-isostatic modelling. *Quat. Sci. Rev.* **19,** 1103-1135 (2000).

Shennan, I. *et al*. Relative sea-level changes, glacial isostatic modelling and ice-sheet reconstructions from the British Isles since the Last Glacial Maximum. *J. Quat. Sci.* **21**, 585-599 (2005).

Simons, M. & Hager, B.H. Localization of the gravity field and the signature of glacial rebound. *Nature* **390**, 500-504 (1997).

Simpson, M.J.R., Milne, G.A., Huybrechts, P. & Long, A.J. Calibrating a glaciological model of the Greenland ice sheet from the Last Glacial Maximum to present-day using field observations of relative sea-level and ice extent. *Quat. Sci. Rev.* **28,** 1631-1657 (2009).

Tarasov, L., Dyke, A.S., Neal, R.M. & Peltier, W.R. A data-calibrated distribution of deglacial chronologies for the North American ice complex from glaciological modelling. *Earth Planet. Sci. Lett.* **315-316,** 30-40 (2012).

Weber, M.E. *et al*. Antarctic deglaciation rewritten – highly dynamic ice-sheet disintegration during meltwater pulses and contribution to sea-level rise. Paper presented at the *PAGES 4th Open Science Meeting, Goa, India* (2013)

van de Plassche, O. (Ed.). *Sea-level Research: A Manual for the Collection and Evaluation of Data.* Geo Books, Norwich (1986).

Weaver, A.J., Saenko, O.A., Clark, P.U. & Mitrovica, J.X. Meltwater pulse 1A from Antarctica as a trigger of the Bølling-Allerød warm interval. *Science* **299,** 1709-1713 (2003).

Whitehouse, P.L., Bentley, M.J. & Le Brocq, A.M. A deglacial model for Antarctica: geological constraints and glaciological modelling as a basis for a new model of Antarctic glacial isostatic adjustment. *Quat. Sci. Rev.* **32,** 1-24 (2012).

Willis, J.K., Chambers, D.P., Kuo, C.-Y., & Shum, C.K. Global Sea Level Rise: Recent Progress and Challenges for the Decade to Come. *Oceanography* **24**(4), 26-35 (2010).

Woodward, R.S. On the form and position of the sea-level. *U.S. Geol. Surv. Bull.***48**, 87-170 (1888).

Yokoyama, Y. *et al*. Timing of the Last Glacial Maximum from observed sea-level minima. *Nature* **406**, 713-716 (2000).